Journal of Electronic Materials (2022) 51:6663–6688
https://doi.org/10.1007/s11664-022-09951-7

TOPICAL COLLECTION: SYNTHESIS AND ADVANCED CHARACTERIZATION OF MAGNETIC OXIDES

Synthesis of Nanostructured Ferrites and Cation Distribution Studies by X-ray Magnetic Circular Dichroism, Mössbauer Spectroscopy, and X-ray Absorption Spectroscopy

Subhajit Nandy[1] · **Mamta Latwal**[2] · **Ganesh Pandey**[3] · **Keun Hwa Chae**[1]

Received: 25 February 2022 / Accepted: 9 September 2022 / Published online: 3 October 2022

Abstract

We present an extensive review of different techniques, such as x-ray magnetic circular dichroism, Mössbauer spectroscopy, and x-ray absorption spectroscopy, for determining the cation distribution in ferrites, and a comparison between these techniques is established. We describe the basic principles of these techniques to find the cation occupancies and highlight the important results obtained from these measurements on ferrite nanoparticles and thin films. Cation distribution, an important characteristic that controls the structural, electrical, and magnetic properties of ferrites, is strongly affected by the synthesis methods. Therefore, various synthesis techniques are reported for preparing ferrite nanoparticles and thin films. A summary correlating these techniques and the cation distribution in ferrite nanoparticles and thin films is presented.

Keywords Ferrites · synthesis · cation distribution · x-ray magnetic circular dichroism · Mössbauer spectroscopy · x-ray absorption spectroscopy

Introduction

The wide range of technological applications of ferrite nanoparticles and thin films in various fields has brought enormous interest by researchers. Ferrites are found to be applicable in various fields, such as sensors,[1] memory,[2] and microwave devices,[3] due to their electrical and magnetic properties. These materials are chemically stable and can be easily synthesized. Recently, ferrite materials with a spinel structure have shown a strong potentiality both academically and technically. Ferrites are mostly known for their magnetic applications in refrigerators, and in loudspeakers as permanent magnets, and soft ferrites are used in electronic devices, such as inductors and transformers. The magnetic behavior and interaction are strongly influenced by the occupancies of metal ions in the spinel structure.[4] The magnetic properties of ferrites are governed by the antiferromagnetic superexchange interaction by Fe^{3+} ions at tetrahedral (A) and octahedral (B) sites. These Fe^{3+} ions create three antiferromagnetic superexchange interactions via O ions, denoted as A-O-A, B-O-B, and A-O-B. In an inverse spinel, Fe^{3+} is present at both A and B sites, whereas Fe^{3+} is present only at the B sites for a normal spinel structure. In the case of normal spinel ferrite, only the B-O-B interaction is present. Thus, the cation occupancies at the A and B sites determine the antiferromagnetic superexchange interactions that control the properties of the ferrites, so that determining the exact cation occupancy in ferrites is important to obtain the origin of their magnetic behavior. For doped spinel ferrites, knowing the occupation sites of the doping ions is crucial for tailoring and improving their magnetic properties.[5] In the case of Zn-doped $MgFe_2O_4$, the Zn^{2+} ions prefer to occupy Fe^{3+} sites and enhance the

✉ Subhajit Nandy
snandy1992@gmail.com

✉ Mamta Latwal
mamta.latwal@gmail.com

[1] Advanced Analysis Center, Korea Institute of Science and Technology, Seoul 02792, Republic of Korea

[2] Department of Chemistry, School of Engineering, University of Petroleum & Energy Studies (UPES), Dehradun, Uttarakhand 248007, India

[3] School of Agriculture, Dev Bhoomi Uttarakhand University, Dehradun, Uttarakhand 248007, India

Fe^{3+}-O^{2-}-Fe^{3+} superexchange interaction, leading to an enhancement of the magnetization. Thus, the growth and characterization of spinel ferrite materials are an emerging area of research. Currently, various methods are available for preparing spinel ferrite nanoparticles and thin films. The structural, magnetic, and electrical properties of the spinel ferrites are controlled by the synthesis methods that introduce various cation distributions in the system. Synchrotron radiation-based x-ray magnetic circular dichroism (XMCD) is a powerful technique for studying cation distribution.[6] This method, along with x-ray absorption spectroscopy measurements, provides information related to the electronic and magnetic properties of nanoparticles and thin films under various temperatures and magnetic fields. The element-selective nature of the measurements facilitates the estimation of the spin and orbital magnetic moments of an atom. Element-specific magnetic hysteresis loops suggest changes in the magnetic properties of ferrite nanoparticles and thin films. Therefore, XMCD studies are crucial for understanding the atomistic origin of magnetization in ferrites, and the effect of cation distribution on their structural, electrical, and magnetic properties. Apart from XMCD studies, other techniques, such as x-ray diffraction,[7] Mössbauer spectroscopy,[8] x-ray absorption spectroscopy,[9] and neutron diffraction,[10] are used to find the cation distribution in ferrites.

XMCD studies have been carried out on various ferrite nanoparticles and thin films prepared by different methods. Room-temperature XMCD studies were performed at Fe and Co $L_{2,3}$ edges on high-quality $CoFe_2O_4$ nanoparticles in total electron yield mode.[11] The Fe and Co cation distribution and their spin and orbital magnetic moments are calculated by simulating the experimental curves and using the sum rule. So, the XMCD is an efficient technique that can provide both cation distribution and magnetic moments of ions. XMCD studies on $CoFe_2O_4$ nanoparticles showed a partial inverse spinel structure with similar cation distribution and stoichiometry for a series of samples.[12] Combined studies of XMCD and magnetization showed different cation distribution and oxygen vacancy concentrations which create local ferromagnetism in $ZnFe_2O_4$ nanoparticles and thin films.[13] It has been reported that the magnetic properties alter with the synthesis methods, and that nanoparticle size depends on the cation distribution in the systems.[14,15] Apart from the XMCD studies, Mössbauer spectroscopy and x-ray absorption spectroscopy are also widely used to determine the cation occupancies in ferrites. Mössbauer spectroscopy is utilized to find the degree of inversion in bulk and nanosized particles of $CuFe_2O_4$, $MnFe_2O_4$, and $NiFe_2O_4$.[15] This technique was used to confirm the structural changes from inverse spinel to normal spinel in the case of $NiFe_{2-x}Cr_xO_4$ and $CoFe_{2-x}Ce_xO_4$ ferrites with increasing the content of Cr and Ce.[16,17] X-ray absorption spectroscopy is used to find the degree of inversion in $MnFe_2O_4$ and $CoFe_2O_4$ and their variation with varying the particle sizes and synthesis methods.[18–20]

In this review article, various synthesis methods for preparing ferrite nanoparticles and thin films, and their effects on structural, physical, and cation distribution properties, are discussed. The variation of cation occupancies in ferrites is reported in terms of various synthesis parameters. Since the cation distribution is an important parameter in defining the physical properties and structural changes of ferrites, various techniques, such as XMCD, Mössbauer spectroscopy, and x-ray absorption spectroscopy, are illustrated in terms of discovering the cation distribution. A detailed discussion of each technique and their comparison are made in this article.

Structure of Ferrites and Metal Ion Occupancy

Ferrite nanoparticles are metal oxides with spinel structure having the general formula, MFe_2O_4 , where M represents divalent metallic cations (M = Co, Ni, Cu, Zn, Mn, or other metals). The word spinel is derived from the mineral $MgAl_2O_4$ due to its structural similarity.[21] In this mineral, oxygen ions are placed at the face centers of a cubic structure. However, Mg^{2+} and Al^{3+} ions occupy tetrahedral and octahedral voids surrounded by oxygen ions (Fig. 1). These metallic cations are positioned at two different crystallographic sites: tetrahedral (A) and octahedral (B). There are 64 tetrahedral and 32 octahedral sites in the spinel structure. One-eighth of the A sites and one-half of the B sites are occupied by metal ions, the rest remain empty. Thus, in the structure, a unit cell contains 8 molecules. In the case of spinel ferrites, Al^{3+} ions are replaced by Fe^{3+}, making the chemical formula MFe_2O_4.[22]

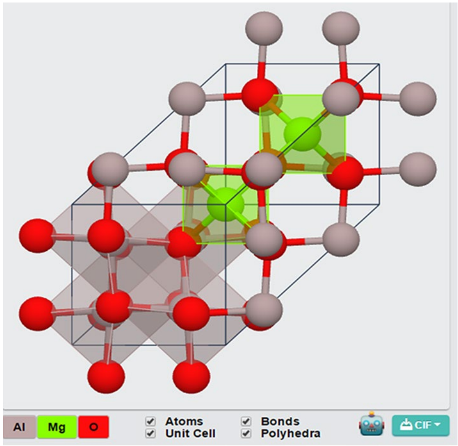

Fig. 1 Spinel structure of $MgAl_2O_4$.

In the case of ferrites, transition metal can occupy either the A or B sites. There are two factors on which the site preference of metals may be determined.

(a) Large ions having low charge prefer A sites.
(b) The difference in the electronic configuration of the cations leads to another set of preference criteria for the A and B sites:
  (i) Ions with filled 3*d* shells like Zn^{2+} tend to form covalent bonds with sp^3 orbitals. Therefore, they occupy the A sites in the spinel.
  (ii) Ions with noble gas structures show no preference for either A or B sites.
  (iii) For a half-filled 3*d* shell with spherical symmetry, the preference will be decided by the influence of the crystalline electric field originating from the neighboring ions on the average energy levels and the spatial distribution of the 3*d* charges.

In ferrites, the chemical bond is assumed to be ionic, to a first approximation. Therefore, the main part of the lattice energy is Coulomb energy and Born repulsive energy. Other factors, such as polarization, individual preference of certain ions for 4-fold and 6-fold coordination, and magnetic interaction, also contribute to lattice energy. These energies depend on the lattice parameter, '*a*', oxygen parameter, 'u', and the cation distribution. According to the cation distribution among the A and B sites, the spinel structure may be classified in the following categories:

(i) Normal spinel structure: 8 M^{2+} ions at A sites and 16 Fe^{3+} ions at B sites. Example: $ZnFe_2O_4$
(ii) Inverse spinel structure: 8 Fe^{3+} ions at A sites and (8 Fe^{3+} + 8 $M.^{2+}$) ions at B sites. Example: $NiFe_2O_4$
(iii) Intermediate or mixed spinel structure: ${Fe_{1-x}}^{3+}{M_x}^{2+}$ at A sites and ${Fe_{1+x}}^{3+}$ ${M_{1-x}}^{2+}$ at B sites. Example: $MnFe_2O_4$

Although categories (i) and (ii) are defined, the examples also show slight deviations from the crystal structure. Thus, most of the ferrites are characterized by a general formula as $({Fe_{1-x}}^{3+}{M_x}^{2+})_A\{{Fe_{1+x}}^{3+}{M_{1-x}}^{2+}\}_B$ to show the distribution of ferrite. This distribution not only affects the structure but also leads to significant changes in the magnetic properties of the ferrite. According to cation distribution, the magnetic moment of ferrite is given as

$$m = \left((1+x)m_{Fe}^{3+} + (1-x)m_M^{2+}\right)_B - \left((1-x)m_{Fe}^{3+} + xm_M^{2+}\right)_A$$

This makes the determination of this distribution extremely important. In general, the distribution is characterized by the presence of Fe^{3+} ions on the A site and is widely termed cation inversion, which is defined as

$$\lambda = \frac{1-x}{1+x}$$

where $x = 1$ for the normal spinel structure, and 0 for the inverse spinel structure, while the value is $0 < x < 1$ for the mixed spinel structure. Keeping in mind the necessities of cation inversion, numerous efforts are being made by researchers to precisely control this factor by synthesis processes. More than this, significant attention is being given to determining this factor by suitable methods. So this review article discusses various synthesis approaches to prepare ferrite nanoparticles and thin films, and their cation distribution studies.

Ferrite Nanoparticle Synthesis

Spinel ferrite nanoparticles are synthesized by various methods, such as mechanical milling, ultrasonics, hydrothermal/solvothermal, micro-emulsion, co-precipitation, microwave-assisted, and sol–gel. The preparation of ferrite nanoparticles by each method is described below.

Mechanical Milling Method

The top–down approach of mechanical milling is used for large-scale production of nanoparticles. A high-energy shaker or ball mill or sometimes tumbler mills are used. The nanoparticles prepared by this method have a random shell and an ordered ferromagnetic core. The limitation of this method is the contamination of the nanoparticles by the milling tools during the milling process, which results in nonstoichiometry in the nanoparticles. Nanocrystalline $NiFe_2O_4$ was successfully synthesized by the reactive milling method using a stoichiometric mixture of commercial nickel and iron oxides.[23] The $NiFe_2O_4$ nanoparticles were found to be disordered and to incorporate defects. It is reported for $NiFe_2O_4$ nanoparticles that the magnetization depends on the milling time and annealing temperature due to the cation reordering in the crystal structure. Magnetization increases initially up to a milling time of 12 h, and reduces with further increasing the milling time after completion of the reaction between the starting oxides.[23] $CuFe_2O_4$ crystals have been prepared by the combined methods of reactive milling, heat treatment, and mechanical milling.[24] The reactive milling contained a stoichiometric mixture of CuO, and α-Fe_2O_3 hematite. $CuFe_2O_4$ was formed at a temperature of 600–1000°C. Finally, mechanical milling was carried out using the same mill, vial, and disc rotational speed to refine the crystalline size of the $CuFe_2O_4$. The magnetization of $CuFe_2O_4$ decreased due to the partial redistribution of the cations in the spinel by increasing the milling time.[24] A mechanochemical process of synthesizing ferrite nanoparticles using a ball mill was investigated by Todaka et al.[25] Different ferrites, such as Fe_3O_4, $CoFe_2O_4$, and $Ni_{0.5}Zn_{0.5}Fe_2O_4$ nanoparticles, were prepared by taking aqueous solutions of various chlorides, $FeCl_3$, $CoCl_2$, or $NiCl_2/ZnCl_2$, and NaOH, in a horizontal ball mill (SUS304). The pH of the solution was controlled by varying the amount of NaOH, and a centrifuge was used to separate the nanoparticles from the solution. A combined approach of microwave-assisted ball milling was introduced for the synthesis of nanocrystalline $NiFe_2O_4$ particles with a mean size of about ~ 20 nm.[26] Nickel carbonate and iron powders were used as precursors. Initially, an intermediate product, $Fe_2Ni_2(OH)_8CO_3.2H_2O$, was formed during the milling process, and this product further reacted to form $NiFe_2O_4$ nanocrystals. $ZnFe_2O_4$ nanoparticles were prepared by mechanical milling using ZnO and α-Fe_2O_3 powder.[27] The powders were placed in a stainless steel vial with a ball-to-powder weight ratio of 10:1. The milling process was carried out at 275 rpm for 50 and 35 h. The effect of lattice constant, inversion degree, and crystallite size on the variation of magnetization was demonstrated. It was reported that cation inversion is the most significant parameter that can most effectively tune the magnetic properties. The saturation magnetization was found to be 79 emu/g at 5 K, with the degree of inversion varying from 0.56 to 0.61.[27] $ZnFe_2O_4$ and $MgFe_2O_4$ nanocrystalline powders were prepared by high-energy milling using a planetary ball mill with a 2×150 grinding chamber and balls made of α-Al_2O_3.[28] The degree of inversion for the $MgFe_2O_4$ decreased with the increasing the milling time. The inversion was found to be 0.904(1) for bulk $MgFe_2O_4$ and changed to 0.856(3) and 0.756(1) with increasing the milling time to 15 and 30 min, respectively. With further increasing the milling time, the degree of inversion saturated at 0.73. In the case of $ZnFe_2O_4$, the degree of inversion was reported to be 0.41.[28] Synthesis parameters for preparing various ferrite nanoparticles by mechanical milling are listed in Table I.

Ultrasonic Method

This method is very popular because of the control of the reaction conditions and particle size distribution. The temperature and intensity of the ultrasonic waves are the two major factors that control the particle size of nanocubes. Here, high-energy collisions between the particles forms the nanocubes which undergo in situ calcination. Ultrasonication is responsible for the mixing at the atomic level and the formation of the crystalline phase at low temperatures. Some examples are cobalt and manganese ferrites.[29,30] Magnetization is shown to be decreased to 21.58 emu/g in Gd^{3+} -substituted $CoFe_2O_4$ compared to 40.19 emu/g in pure $CoFe_2O_4$ nanoparticles. On the other hand, electrical properties, such as dielectric constant and ac conductivity, increased in Gd^{3+} -substituted $CoFe_2O_4$ nanoparticles. The cation distribution in Gd^{3+} -substituted $CoFe_2O_4$ nanoparticles prepared by the sonochemical method plays a significant role in determining these physical properties.[29] The cation distribution was found to be varied in $MnFe_2O_4$ nanoparticles with the variation of sonication time. The formula of $MnFe_2O_4$ is reported as $(Mn_{0.29}Fe_{0.42})[Mn_{0.71}Fe_{1.58}]O_4$ and $(Mn_{0.28}Fe_{0.54})[Mn_{0.72}Fe_{1.46}]O_4$ for sonication times of 20 and 80 min, respectively. The saturation magnetization was enhanced from 1.9 emu/g to 52.5 emu/g with increasing sonication time from 20 to 80 min. These changes are attributed to the cation occupancies in the $MnFe_2O_4$ nanoparticles.[30] Sonochemical syntheses of $CoFe_2O_4$ were carried out in which cobalt acetate and iron acetate were placed (1:2 ratios) in millipore water.[31] The solution was kept on a sonicator for 30 min at 70°C. The pH ~ 4.5 was maintained with 0.1 N NaOH or 0.1 N HCl. The chemical reactions of $CoFe_2O_4$ synthesis were:[31]

$$Fe\left(CH_3COO\right)_2 + H_2O_2 \rightarrow Fe(OH)_2 + 2CH_3COOH$$

$$3Fe(OH)_2 + H_2O_2 \rightarrow Fe_3O_4 + 4H_2O$$

Table I Selected ferrite nanoparticles synthesized by mechanical milling

Nanoparticle	Synthesis parameters					Crystallite size	References
	Precursor	Weight ratio (ball: powder)	Milling time	Vial rotational speed	Annealing temperature and time		
$NiFe_2O_4$	NiO, α-Fe_2O_3	15:1	4–30 h	800 rpm	350°C, 4 h	9–39 nm	Marinca et al.[23] (2011)
$CuFe_2O_4$	CuO, α-Fe_2O_3	11:1	4–30 h	800 rpm	600–1000°C, 4 h	6–9 nm	Marinca et al.[24] (2012)
Fe_3O_4	$FeCl_3$, NaOH	–	24–120 h	–	52.4°C	20–100 nm	Todaka et al.[25] (2003)
$CoFe_2O_4$	$CoCl_2$, $FeCl_3$, NaOH	–	72 h	–	–	30 nm	Todaka et al.[25] (2003)
$Ni_{0.5}Zn_{0.5}Fe_2O_4$	$NiCl_2$/ $ZnCl_2$, $FeCl_3$, NaOH	–	96 h	–	–	30 nm	Todaka et al.[25] (2003)
$NiFe_2O_4$	$NiCO_3.2Ni(OH)_2.4H_2O$, Fe powder	8:1	30 min	200–400 rpm	50°C, 12 h	20 nm	Chen et al.[26] (2012)
$ZnFe_2O_4$	ZnO, α-Fe_2O_3	10:1	150 h	275 rpm	–	12 nm	Cobos et al.[27] (2020)
$MgFe_2O_4$	MgO, α-Fe_2O_3	50:1	–	750 rpm	–	–	Šepelák et al.[28] (2004)
$ZnFe_2O_4$	ZnO, α-Fe_2O_3	50:1	–	750 rpm	–	–	Šepelák et al.[28] (2004)

$$\mathrm{Co}\left(\mathrm{CH_3COO}\right)_2 + 2\mathrm{H_2O} \rightarrow \mathrm{CoO} + 2\mathrm{CH_3COOH} + 2\mathrm{H_2O}$$

$$2\mathrm{Fe_3O_4} + 3\mathrm{CoO} \rightarrow^{[O]} 3\mathrm{CoFe_2O_4} \text{ (in presence of ultrasound)}$$

A simple and easy technique of ultrasonic cavitation-induced water in vegetable oil emulsion droplets was used to synthesize manganese zinc ferrite nanocrystals.[32] This method consists of rapeseed oil as an oil phase and an aqueous solution of Mn^{2+}, Zn^{2+}, and Fe^{2+} acetate. The reaction was performed at 300°C for 3 h, so that the small amount of oil present on the surface of the ferrite could be eliminated. The prepared manganese zinc ferrite was nanocrystalline. Another method of ultrasonic-assisted synthesis of self-assembled $CuFe_2O_4$ nanoparticles was also reported by Abbasian et al., [33] in which $FeCl_3.6H_2O$, $CuCl_2.2H_2O$, and sodium acetate were used as precursors. The solution was stirred and exposed to ultrasonic waves. Finally, centrifuging, washing, and drying were carried out to obtain $CuFe_2O_4$ nanoparticles. The ferrites synthesized by ultrasonic methods are listed in Table II.

Hydrothermal/Solvothermal Method

This method is well known because different sizes, shapes, and morphologies of ferrite nanoparticles can be prepared by controlling the experimental parameters.[37] It is also known as an economical and eco-friendly method, due to the use of water as a solvent. Using this method, various ferrites nanoparticles, such as multiwalled carbon nanotube $CoFe_2O_4$, Fe_3O_4, $CoFe_2O_4$, Ni-Zn ferrite, $MnFe_2O_4$, and metal-doped $MgFe_2O_4$ have been synthesized.[38–40] $Co_{1-x}Ni_xFe_2O_4$ nanoparticles were successfully prepared by this method using ethylene glycol as solvent.[41] $Co(NO_3)_2.6H_2O/Ni(NO_3)_2.6H_2O$, and $Fe(NO_3)_3.9H_2O$ as precursors were taken in a 1:2 molar ratio and dissolved in ethylene glycol. Anhydrous sodium acetate and polyethylene glycol were added to the mixture and stirred continuously for 30 min. The mixture was kept in an autoclave at 200°C for 12 h and then cooled to room temperature. The final product was washed with distilled water and anhydrous ethanol and dried at 70°C for 12 h under vacuum.[41] Cobalt ferrite nanoparticles have been synthesized

Table II Selected ferrite nanoparticles, their synthesis parameters, and crystallite size using ultrasonic methods

Nanoparticle	Synthesis parameters				Crystallite size	Reference
	Precursor	Reaction temp.	Ultrasonication time	Freq. and power		
$CoFe_{2-x}Gd_xO_4$ ($x = 0$–0.2)	$Co(NO_3)_2.6H_2O$ $Fe(NO_3)_3.9H_2O$ $Gd(NO_3)_3{\cdot}6H_2O$	90°C	60 min	20 kHz, 70 W	9.2–7.6 nm	Yadav et al.[29] (2018)
$MnFe_2O_4$	$Mn(NO_3)_2{\cdot}4H_2O$ $Fe(NO_3)_2{\cdot}9H_2O$ NaOH	–	20–80 min	20 kHz, 70 W	19.3–25.5 nm	Yadav et al.[30] (2020)
$CoFe_2O_4$	Cobalt acetate tetrahydrate, iron (II) acetate, NaOH pellets	70°C	24 min	20 kHz, 100 W	24 nm	Goswami et al.[31] (2013)
$Mn_{0.5}Zn_{0.5}Fe_2O_4$	Consisting of rapeseed oil as an oil phase and aqueous solution of Mn^{2+}, Zn^{2+} and Fe^{2+} acetate	25–30°C	20 min	20 kHz, 70 W	20 nm	Sivakumar *et al*[32] (2012)
$CuFe_2O_4$	$FeCl_3$ $.6H_2O$, $CuCl_2$ $.2H_2O$ and sodium acetate	–	30 min	20 kHz, 350 W	12.4 nm	Abbasian et al.[33] (2020)
Cu doped $NiMnFe_2O_4$ ($x = 0.1$–0.4)	$Fe(NO_3)_3.9H_2O$, $Ni(NO_3)_2.6H_2O$, $MnSO_4.H_2O$ and $Cu(NO_3)_2.3H_2O$	80°C	60 min	20 kHz	19–23 nm	Amulya et al.[34] (2020)
$MnFe_2O_4$	$MnAc_2.2H_2O$ $FeAc_2$, NaOH, HCl	70°C	30 min	20 kHz, 100 W	34–46 nm	Goswami et al.[35] (2013)
$ZnFe_2O_4$	$ZnAc_2.2H_2O$, $FeAc_2$, H_2O_2, NH_4OH	70°C	1 h	35 kHz, 35 W	6–17 nm	Choudhury et al.[36] (2013)

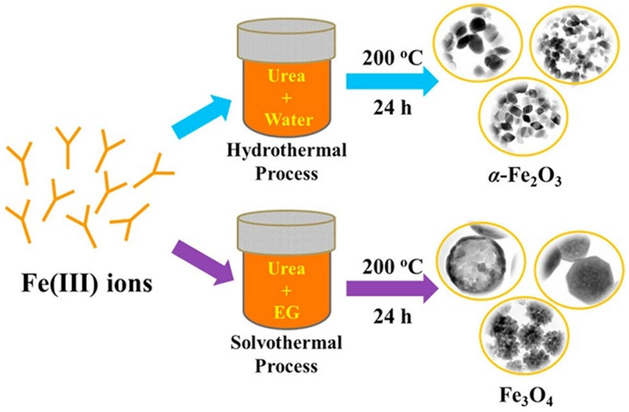

Fig. 2 Synthesis of α-Fe_2O_3 and Fe_3O_4 nano- and microstructures by the hydrothermal/solvothermal process; reprinted from Ref. 44 with permission from Elsevier.[44]

by the solvothermal method.[42] $Co(NO_3)_2.6H_2O$ and $Fe(NO_3)_3.9H_2O$ were mixed with 3 M NaOH solution in deionized water. The solution was mixed by simultaneous heating and stirring, then transferred into an autoclave. Finally, the nanoparticles were washed, dried, and calcinated. Various nanoparticles of MFe_2O_4 (M = Mn, Co, Ni) have been synthesized by the hydrothermal method.[43] For the preparation of 0.1 g ferrite, $MnAc_2$ was mixed with $FeAc_2$ and dissolved in a suitable solvent, such as benzyl alcohol or hexanol. The resulting solution was stirred and crystallized at 180°C for 24 h. Finally, the autoclave was cooled to room temperature and the sample was centrifuged at 5000 rpm for 30 min. The product was washed with ethanol and dried at room temperature.[43] A facile synthesis of α-Fe_2O_3 and Fe_3O_4 nano- and microstructures by the hydrothermal/solvothermal process is shown in Fig. 2.[44] The process involved in the morphology and size-control with the role of the reaction medium was also studied.

Superparamagnetic $ZnFe_2O_4$ submicron spheres were prepared by the one-pot solvothermal method.[45] In this preparation, $ZnCl_2$, $FeCl_3$, and CH_3COONa were used as precursors and ethylene glycol was taken as a solvent. The solution was kept in an autoclave at 200–215°C for 4–8 h. The autoclave was cooled to room temperature before collecting the $ZnFe_2O_4$ nanocrystals, which were finally washed with deionized water and ethanol and dried at 60°C. A one-step hydrothermal method for the synthesis of $CuFe_2O_4$/reduced graphene oxide aerogel was reported by Yao et al.[46] The observed properties, such as high efficiency, good reusability, and a simple synthesis process, make this aerogel a promising catalyst for wastewater treatment. Saturation magnetization increases in Cu-substituted $CoFe_2O_4$ nanoparticles with increasing Cu content up to 0.3, and decreases with larger Cu content. These changes are attributed to the crystallinity, cation distribution, misbalance of Fe^{3+} ions in

Table III Synthesis parameters and nanoparticle sizes of selected ferrites using the hydrothermal/solvothermal method

Nanoparticle	Synthesis parameters				Particle/crystallite size	Reference
	Precursors	Solvent	Temp.	Time		
$Ni_xZn_{1-x}Fe_2O_4$	$FeCl_3{\cdot}6H_2O$, $Zn(NO_3)_2.6H_2O$, $Ni(NO_3)_2.6H_2O$	Ethylene glycol	160–220°C	2–12 h	–	Ni et al.[38] (2015)
$MnFe_2O_4$	$FeCl_3{\cdot}6H_2O$, $Mn(CH_3COO)_2{\cdot}4H_2O$, $MnCl_2{\cdot}4H_2O$	Ethylene glycol	200°C	12 h	230–950 nm	Li et al.[39] (2015)
$MgFe_2O_4$/graphene	$MgCl_2.6H_2O$, $FeCl_3.9H_2O$	Ethylene glycol	60°C	24 h	100–160 nm	Yin et al.[40] (2017)
$Co_{1-x}Ni_xFe_2O_4$	$Co(NO_3)_2.6H_2O$, $Ni(NO_3)_2.6H_2O$, $Fe(NO_3)_2.9H_2O$	Ethylene glycol	200°C	12 h	40–90 nm	Tang et al.[41] (2012)
$CoFe_2O_4$	$Co(NO_3)_2.6H_2O$, $Fe(NO_3)_2.9H_2O$	Deionized water	150°C	6 h	34 nm	Allaedini et al.[42] (2015)
MFe_2O_4 (M = Mn, Co and Ni)	$Mn(acac)_2$, $Fe(acac)_2$, Ni $(acac)_2$, $Co(acac)_2$	Hexanol	180°C	24 h	5–10 nm	Vilar et al.[43] (2009)
α-Fe_2O_3 and Fe_3O_4	$FeCl_3.6H_2O$	Deionized water	200°C	24 h	60–100 nm	Su et al.[44] (2016)
$ZnFe_2O_4$	$FeCl_3.6H_2O$, $ZnCl_2$	Ethylene glycol	200–215°C	4–8 h	375–500 nm	Ma et al.[45] (2017)
$CuFe_2O_4$ reduced graphene oxide	$Cu(NO_3)_2.3H_2O$, $Fe(NO_3)_2.9H_2O$	Deionized water	180°C	8 h	50 nm	Yao et al.[46] (2019)
$Co_{1-x}Cu_xFe_2O_4$ ($x = 0$, 0.3, 0.7)	$Co(NO_3)_2.6H_2O$, $Fe(NO_3)_3.9H_2O$, $CuSO_4.5H_2O$	Deionized water	65°C	15–30 min	15–30 nm	Aswad et al.[47] (2021)

tetrahedral and octahedral sites, and super-exchange interaction.[47] A list of different ferrite nanoparticles prepared by the hydro(solvo) thermal method is given in Table III.

Micro-emulsion Method

This method of ferrite nanoparticle synthesis is known for its environmentally friendliness and the size-controlled nature of the nanoparticles. It requires a low temperature and a large amount of solvent, reuses the surfactant several times. One of the main drawbacks of this method is the poor crystalline nature of the nanoparticles. Preparation of nanoparticles of barium ferrite using the micro-emulsion method was investigated by Palla et al.[48] The precursor carbonate and hydroxide can be precipitated by the aqueous cores of the water-in-oil micro-emulsion method. The prepared precursor was calcinated at 925°C for 12 h. After 12 h, the product was transferred to hexagonal ferrite. The pH of the reaction was maintained between 5 and 12, affecting the magnetic properties of the particles. It was reported that the barium ferrite crystals prepared by the micro-emulsion method had both higher intrinsic coercivity and saturation magnetization. Neodymium-doped $LiNi_{0.5}Fe_2O_4$ nano-crystalline was prepared via micro-emulsion.[49] The preparation of ferrite nanoparticles by the oil-in-water micro-emulsion method was carried out by organometallic precursors by mixing with a surfactant, oil component, and Milli-Q-water.[50] All the components were mixed at 25°C and stirred until a brown transparent micro-emulsion was formed. Finally, centrifugation and washing were carried out with a water and ethanol mixture (1:1) and drying in the oven at 70°C for 2 days to obtain Mn-Zn ferrite nanoparticles. In $Mg_{1-x}Ca_xNi_yFe_{2-y}O_4$ nanoparticles synthesized by the micro-emulsion method, the saturation magnetization increased from 9.84 to 24.99 emu/g with increasing Ca and Ni content up to $x = 0.2$ and $y = 0.4$, while the dielectric constant decreased with increasing Ca-Ni concentration. These changes were attributed to the cation distribution in $Mg_{1-x}Ca_xNi_yFe_{2-y}O_4$ with changing the Ca-Ni content. It has been shown that Ca and Ni prefer to occupy octahedral sites, while Fe^{3+} migrates from octahedral to tetrahedral sites.[51] Similarly, magnetization values increased from 20.5 to 47.6 emu/g with increasing x in $Ni_{0.5}Sn_{0.5}Co_xMn_xFe_{2-2x}O_4$ ferrites. The origin of the magnetization is the imbalance of the magnetic moments at the tetrahedral and octahedral sites. As the cation distribution depends on the ionic radii of the cations, introducing different cations into the structure causes changes in the magnetic moments.[52] A list of different ferrite nanoparticles prepared by the micro-emulsion method is given in Table IV.

Co-precipitation Method

Co-precipitation is an easy method to perform economically to obtain high mass production in less time. Various spinel ferrite nanoparticles have been synthesized by this method to get uniform-sized nanoparticles. A careful observation of the pH in the solution is needed to get good quality nanocubes. For the preparation of nickel ferrite nanoparticles, the co-precipitation method is very popular and easy.[57] The flow chart of nickel ferrite preparation by this method is as follows (Fig. 3).

Nano-spinel ferrites ($Ni_{0.4}Cu_{0.2}Zn_{0.4}Fe_2O_4$) were prepared by co-precipitation assisted by ultrasonic irradiation produced by an ultrasonic cleaner with a frequency of 20 kHz.[58] Chlorinated salts and KOH were used as the initial materials. The microstructure and magnetic properties dependence on the ultrasonic power and reaction temperature were studied. X-ray diffraction studies confirmed the formation of pure $(NiCuZn)Fe_2O_4$ ferrite nano-spinel with crystallite sizes of less than 40 nm and a lattice constant of 8.39 Å. Nanoparticles of $MnFe_2O_4$ with different sizes by varying the pH have been prepared by chemical co-precipitation.[59] These nanoparticles were modified on their surfaces with polysaccharide chitosan to discover the characteristics of hyperthermia and magnetic resonance imaging (MRI). The sizes of the $MnFe_2O_4$ particles varied from 5 to 15 nm at pH 9–12. The hydrodynamic sizes were less than 250 nm, with a polydispersity index of 0.3, and zeta potentials were higher than 30 mV, which proved the electrostatic repulsion for a stable colloidal suspension. The MRI properties at 7 T described that the transverse relaxation (T2) doubled as the size of the CS-coated $MnFe_2O_4$ nanoparticles tripled in vitro. However, through the study of in vivo positive contrast MRI angiography, the longitudinal relaxation (T1) was strongest for the smallest CS-coated $MnFe_2O_4$ nanoparticles. Finally, the results showed the exciting potential of CS-coated $MnFe_2O_4$ nanoparticles in MRI and of hyperthermia studies for biomedical research. $CoFe_2O_4$ and $ZnCoFe_2O_4$ have been prepared by a modified co-precipitation method,[60] which was reported to be a simple, environment-friendly, and low-temperature process in which no oxidizing or coating agent was used. The composition of the precursor materials was also changed (molar ratio of Fe^{+3}:Fe^{+2}:Co^{+2}/Zn^{+2} of 3:2:1). Ferrites synthesized by the co-precipitation method are listed in Table V. $Sn_{1-x}Mn_xFe_2O_4$ nanoparticles, synthesized by co-precipitation method, showed increasing magnetization and coercive fields with increasing the content of Mn in $SnFe_2O_4$. These changes were attributed to the increasing degree of inversion of Fe^{3+} and the decreasing degree of inversion for Mn^{2+} ions.[61]

Table IV Ferrite nanoparticles prepared by micro-emulsion method

Nanoparticle	Synthesis parameters			Particle/crystallite size	Reference
	Precursors	Solvent	Annealing temp. and time		
$BaFe_{12}O_{19}$	$(Fe(NO_3)_3$, $(Ba(NO_3)_2$, C-TAB	NaOH, Na_2CO_3	925°C (12 h)	3–8 nm	Palla et al.[48] (1999)
$LiNi_{0.5}Nd_xFe_{2-x}O_4$	$Fe(NO_3)_2.9H_2O$, $NiCl_2.6H_2O$, CTAB, $Nd(NO_3)_3.6H_2O$	Distilled water	950°C (-)	30–120 nm	Gilani et al.[49] (2017)
Mn-Zn ferrite	Mn, Zn, Fe ethylhexanoate	Isopropa-nol, NaOH	70°C (48 h)	6–12 nm	Pemartin et al.[50] (2014)
$Mg_{1-x}Ca_xNi_yFe_{2-y}O_4$	$Fe(NO_3)_2.9H_2O$, $CaCl_2.2H_2O$, $MgSO_4.7H_2O$, $NiCl_2.6H_2O$	Aqueous NH_3	700°C (7 h)	29–45 nm	Ali et al.[51] (2014)
$Ni_{0.5}Sn_{0.5}Co_xMn_xFe_{2-2x}O_4$	$Ni(NO_3)_2.6H_2O$, $Co(NO_3)_2.6H_2O$, $SnCl_2{\cdot}2H_2O$, MnO_2 and $FeCl_3$, Cetyltrimethylammonium	Aqueous NH_3	950°C (6 h)	11.8–19.7 nm	Ali et al.[52] (2017)
$Mg_{1-x}Ni_xCo_yFe_{2-y}O_4$	$MgSO_4.7H_2O$, $NiCl_2.6H_2O$, $CoCl_2.6H_2O$, $Fe(NO_3)_2.9H_2O$	Aqueous NH_3	700°C (7 h)	15–26 nm	Ali et al.[53] (2014)
$Y_xMnFe_{2-x}O_4$	$Fe(NO_3)_2.9H_2O$, $Mn(CH_3COO)_2{\cdot}4H_2O$	1-butanol, NaOH	400°C (4 h)	–	Yousuf et al.[54] (2020)
Cr-substituted $MnFe_2O_4$	$Fe(NO_3)_2.9H_2O$, $Mn(CH_3COO)_2{\cdot}4H_2O$, $Cr(NO_3)_2.9H_2O$	1-butanol, NaOH	400°C (4 h)	6–15 nm	Yousuf et al.[55] (2019)
$Ni_{0.6}Co_{0.2}Zn_{0.2}Fe_{2-y}La_yO_4$	$Ni(NO_3)_2.6H_2O$, $Co(NO_3)_2.6H_2O$, $Zn(NO_3)_2.6H_2O$, $Fe(NO_3)_3.9H_2O$, $La(NO_3)_3.5H_2O$	Double-distilled water	60°C (3 h)	20 nm	Ganure et al.[56] (2017)

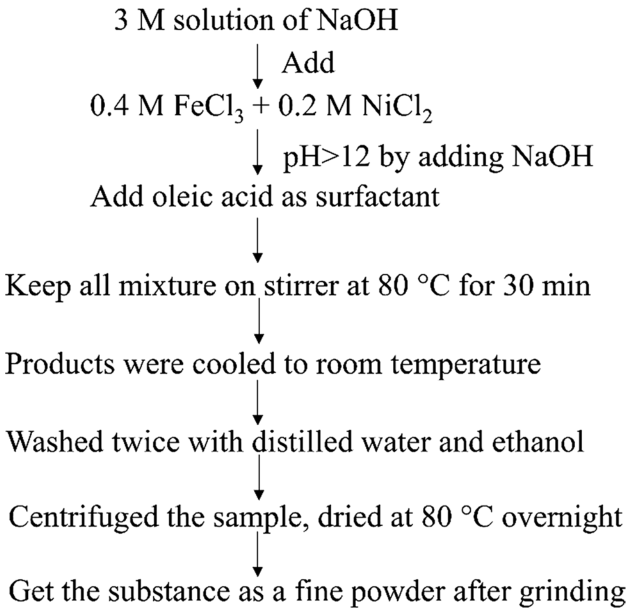

Fig. 3 Flow chart of $NiFe_2O_4$ nanoparticles synthesis by co-precipitation.

Microwave-Assisted Method

This method is a new technique, that is fast, simple to use, has a high yield, low cost, and shorter reaction time, in which microwave energy is used for the combustion of precursors. During the reaction, the microwave energy is converted into thermal energy and the temperature rises for a shorter period at 100–200°C. The common ferrites prepared by this method are Fe_3O_4, $NiFe_2O_4$, $CoFe_2O_4$, $Mn_{1-x}Ni_xFe_2O_4$, and $ZnFe_2O_4$.[64,65] Nanocrystalline $NiFe_2O_4$ and $CoFe_2O_4$ have been prepared by the microwave-assisted combustion process. The stoichiometric proportion of nickel nitrate hexahydrate $(Ni(NO_3)_2.6H_2O)$, ferric nitrate nonahydrate $(Fe(NO_3)_3.9H_2O)$, and urea NH_2CONH_2 were dissolved in deionized water. The solution was kept in a crucible in a microwave oven. At first, the solution boiled and underwent dehydration and decomposition with a large number of gases. As a point of spontaneous combustion was achieved, the solution began to burn, a great deal of heat was released,

Table V Selected ferrite nanoparticles and their synthesis parameters using the co-precipitation method

Nanoparticle	Synthesis parameters			Particle/crystallite size	Reference
	Precursors	Temp.	Time		
$NiFe_2O_4$	$FeCl_3$, $NiCl_2$, NaOH	80°C	30 min	16 nm	Sagadevan et al.[57] (2018)
$Ni_{0.4}Cu_{0.2}Zn_{0.4}\ Fe_2O_4$	$NiCl_2·6H_2O$, $CuCl_2·6H_2O$, $ZnCl_2$, $FeCl_3·6H_2O$	25°C	25 min	40 nm	Peng et al.[58] (2021)
$MnFe_2O_4$	$MnCl_2·4H_2O$, $FeCl_3$, NH_4OH	25°C	20 min	5–15 nm	Islam et al.[59] (2020)
$CoFe_2O_4$ and $ZnCoFe_2O_4$	$FeCl_3.6H_2O$, $FeCl_2.4H_2O$,$CoCl_2.6H_2O$, $ZnCl_2$, NH_4OH	60°C	30 min	50.9 and 575 nm	Darwish et al.[60] (2019)
$Sn_{1-x}Mn_xFe_2O_4$	$FeCl_3$, $MnCl_2$ and $SnCl_2$	80°C	30 min	4–9 nm	Moussaoui et al.[61] (2016)
$Co_xFe_{3-x}O_4$	$CoCl_2.6H_2O$, $FeSO_4.7H_2O$	90°C	–	35–60 nm	Olsson et al.[62] (2005)
MFe_2O_4 (M = Fe, Co, Mn)	$CoCl_2.6H_2O$, $MnCl_2.6H_2O$, $FeCl_2.6H_2O$	100°C	2 h	4–12 nm	Pereira et al.[63] (2012)

and all the solution was vaporized and became a solid. The reaction of combustion reaction to getting $NiFe_2O_4$ is:

$$\begin{aligned} \mathrm{Ni}\left(\mathrm{NO_3}\right)_2 \cdot 6\mathrm{H_2O(s)} + 2\mathrm{Fe}\left(\mathrm{NO_3}\right)_3.9\mathrm{H_2O(s)} \\ + 7\mathrm{CO}\left(\mathrm{NH_2}\right)_2\mathrm{(s)} + \frac{3}{2}\mathrm{O_2(g)} \\ \rightarrow \mathrm{NiFe_2O_4(s)} + 11\mathrm{N_2(g)} \\ + 38\mathrm{H_2O(g)} + 7\mathrm{CO_2(g)} \end{aligned}$$

Nanoplatelets of nickel ferrite were synthesized through a microwave-assisted combustion process with the help of trisodium citrate as fuel.[66] Cobalt ferrite nanoparticles by the microwave-assisted solvothermal method were investigated by Kozakova et al.[67] For the synthesis of $CoFe_2O_4$ nanoparticles, $CoCl_2$ and $FeCl_3$ were dissolved in ethylene glycol and mixed. The resulting solution was placed into the microwave at 220°C and at a pressure of about 900 kPa for 30 min. A black product was obtained after cooling to room temperature. The product was rinsed with demineralized water or ethanol and dried at 60°C for 6 h. The microwave-assisted synthesis of water-soluble styrylpyridine dye-capped zinc oxide nanoparticles was investigated by Giridhar et al.[68] $M_xFe_{3-x}O_4$ magnetic ferrite (M = Fe, Mn, Co) spherolites of high surface area have been successfully prepared by a facial microwave-assisted reflux method.[69]

Sol–Gel Method

This method is commonly used for synthesizing ferrite nanoparticles because of its simplicity and cost-effectiveness. The distribution of the nanoparticle sizes can be easily controlled using this method. For the preparation of ferrite nanoparticles by the sol–gel method (Fig. 4), the nitrates of the particular metal ions and a suitable chelating agent, e.g., urea/citric acid, and glycine were taken in the ratio of 1:x (where $x = 1–3$ in most cases). First, the metal nitrate was dissolved in deionized water. Then, the aqueous solution of citric acid was mixed into the metal nitrates. Finally, the mixture was kept on a hot plate at 100°C with continuous stirring until it became gel-like. After some time, the gel itself ignited and burnt at a high temperature. The ignition and decomposition process gives chromium-substituted cobalt ferrite.[70]

Magnetic $MnFe_2O_4$ spinel ferrite nanoparticles were synthesized from metal nitrates by the sol–gel method.[71] A 50% solution of $Mn(NO_3)_2$ and $Fe(NO_3)_3.9H_2O$ powders were mixed with deionized water. The complexing agent (citric acid) was added to the metal nitrate solution with a 1:1 molar ratio. The solution was evaporated and decomposed at 200°C by forming a gel. Finally, calcination was carried out in air at a different temperature to obtain the $MnFe_2O_4$ nanoparticles. An aqueous glycolate sol–gel method was

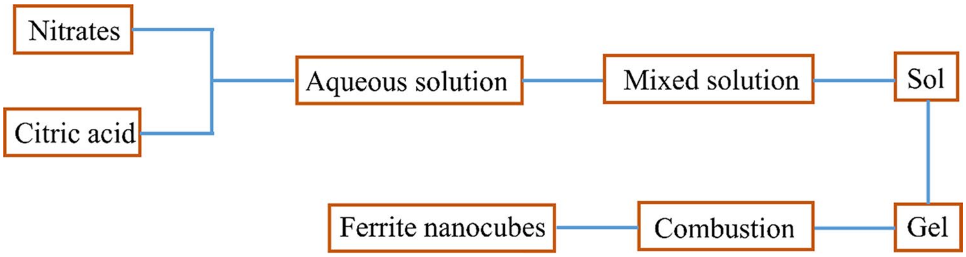

Fig. 4 Flow chart for the formation of ferrite nanocubes.

Table VI Selected ferrite nanoparticles and their synthesis parameters using the sol–gel method

Nanoparticle	Synthesis parameters			Particle/crystallite size	Reference
	Precursors	Solvent	Annealing temperature and duration		
$NiFe_2O_4$	$Fe(NO_3)_3.9H_2O$ $Ni(NO_3)_2.9H_2O$	Distilled water	800 and 1100°C (2 h)	20–450 nm	Yadav et al.[74] (2017)
$ZnFe_2O_4$	$Zn(NO_3)_2.6H_2O$ $Fe(NO_3)_3.9H_2O$	Deionized water	500–1000°C (2 h)	11–57 nm	Yadav et al.[75] (2017)
$Mn_{0.85}Zn_{0.15}Ni_xFe_2O_4$	$MnC_6H_9O_6.(H_2O)_2$, $Zn(NO_3)_2$, $Ni(NO_3)_2$, $Fe(NO_3)_3$	Distilled water	1200°C (5 h)	10–18 nm	Jalaiah et al.[76] (2017)
$Co_{1-x}Zn_xFe_2O_4$	$Fe(NO_3)_3.9H_2O$ $Co(NO_3)_2.6H_2O$ $Zn(NO_3)_2.6H_2O$	Distilled water	800°C (2 h)	19–42 nm	Yadav et al.[77] (2015)
$Mg_{0.7-x}Ni_xZn_{0.3}Fe_2O_4$	$Mg(NO_3)_2{\cdot}6H_2O$ $Ni(NO_3)_2.6H_2O$ $Zn(NO_3)_2.6H_2O$ $Fe(NO_3)_3.9H_2O$	Distilled water	400 and 700°C (2 h)	19–29 nm	Bobade et al.[78] (2012)
$NiCoFe_{2-x}Al_xO_4$	$Fe(NO_3)_3.9H_2O$ $Ni(NO_3)_2$ $Co(NO_3)_2$ $Al(NO_3)_3.9H_2O$	Deionized water	600°C (3 h)	14–17 nm	Khalid et al.[79] (2021)

used to synthesize transition metal ferrite ceramic samples ($YFeO_3$, $Y_3Fe_5O_{12}$, $CoFe_2O_4$, $NiFe_2O_4$, and $ZnFe_2O_4$).[72] Different spinel metal ferrites have been synthesized through the sol–gel combustion method, and the effect of these ferrite nanoparticles on the growth of the microalgae *Picochlorum* sp. has been examined.[73] The prepared metal ferrites were found to possess a high crystalline structure, and the average crystallite sizes of $FeCr_2O_4$, $CoFe_2O_4$, $NiFe_2O_4$, $CuFe_2O_4$, and $ZnFe_2O_4$ were determined as 34, 33, 36, 35, and 52 nm, respectively. The microalgae culture of *Picochlorum* sp. treated with different ferrite nanoparticles showed a significant difference in viable cell concentrations at 48 h and 72 h of incubation as compared to the control samples. However, the growth pattern of both treated and untreated samples was similar. This could indicate that the synthesized nanoparticles may reduce the growth of the microalgae, but will not cause severe inhibition when used at the proper concentration. $NiFe_2O_4$ nanoparticles, synthesized by honey-mediated sol–gel combustion show, an enhanced magnetization with increasing the crystallite size. The magnetization was shown to increase from 32.3 emu/g to 49.9 emu/g and the coercivity decreased from 162 to 47 Oe with the crystallite size increasing from 20 to 163 nm during annealing. This enhancement has also been attributed to the cation occupancies obtained for the as-prepared and air-annealed $NiFe_2O_4$ nanoparticles.[74] The variation of conductivity with increasing the annealing temperature of $ZnFe_2O_4$ nanoparticles has been demonstrated as the variation of the microstructure and mobility associated with cation redistribution.[75] A few selected ferrites prepared by the sol–gel method are listed in Table VI.

Other frequently employed synthesis techniques, such as solid-state,[80] sonochemical,[30] and template methods[81] were used to prepare ferrite nanoparticles.

Ferrite Thin Films Synthesis

Spinel ferrite thin films are grown by using two major techniques. These techniques are based on (1) physical, and (2) chemical deposition methods.

Physical Deposition Method

The extensively used physical deposition methods are sputter deposition and pulsed laser deposition (PLD) for spinel ferrite thin film fabrication. A rapid cooling process from the vapor phase to the solid-state phase in sputtering and PLD introduces a random distribution of metal cations in spinel ferrite thin films.

Sputter Deposition

The sputter deposition technique operated in direct current (DC) and radio frequency (RF) modes is a simple and straight forward process for depositing uniform and dense spinel ferrite compounds. Spinel ferrite $ZnFe_2O_4$ thin films were prepared on various substrates like glass, quartz, Si (100), $SrTiO_3$ (100), and yttria-stabilized zirconia (111) using an RF magnetron sputtering system.[82–85] A ceramic

Table VII Ferrite thin films grown by the sputter deposition method

Thin films prepared	Substrates used	Thickness of the films (nm)	Power applied (W)	Deposition pressure (mTorr)	References
$ZnFe_2O_4$	Glass	300	100	27	Sultan et al.[82] (2009)
$ZnFe_2O_4$	Si (100)	125	–	30	Liang et al.[83] (2013)
$ZnFe_2O_4$	Glass	1060	100	27	Nakashima et al.[84] (2004)
$ZnFe_2O_4$	Quartz	–	100	5.4	Bohra et al.[85] (2006)
$CoFe_2O_4$	$MgAl_2O_4$ (110)	107	100	3.75	Niizeki et al.[86] (2015)
$Co_xFe_{3-x}O_4$ (001)	MgO (001)	40	100	–	Yanagihara et al.[87] (2014)
$Co_xFe_{3-x}O_4$ (001)	MgO (001)	10–60	100	3.75	Niizeki et al.[88] (2013)
$CuFe_2O_4$	Glass	300	–	–	Haija et al.[89] (2016)
$CuFe_2O_4$	Quartz	450	200	4.5	Desai et al.[90] (2002)
$CuFe_2O_4$	Quartz	100	50 and 200	–	Višňovský et al.[91] (2005)
$Mn_{0.6}Zn_{0.4}Fe_2O_4$	Glass	–	–	2	Nakagawa et al.[92] (2003)
$Mn_{0.5}Zn_{0.5}Fe_2O_4$	Si (100)	300	–	8.25	Wang et al.[93] (2008)
$Ni_xZn_{1-x}Fe_2O_4$	Glass	300	60–150	10–50	Lee et al.[94] (1999)
$Ni_xZn_{1-x}Fe_2O_4$	Si (100) Si (111)	50	50	2.25×10^{-3}	Koblischka et al.[95] (2008)
$Ni_{0.5}Zn_{0.5}$ Fe_2O_4	Quartz Si (100)	450	220	4.5×10^{-3}	Desai et al.[96] (2002)
$Ni_xZn_{1-x}Fe_2O_4$	Si (111)	1500	–	15×10^{-3}	Guo et al.[97] (2009)
$Ni_{0.45}Zn_{0.55}Fe_2O_4$	Si (111)	300	–	15×10^{-3}	Guo et al.[98] (2010)
$Ni_{0.5}Zn_{0.5}$ Fe_2O_4	$Pt/Ti/SiO_2/Si$	200	–	18.75×10^{-3}	Wu et al.[99] (2019)
$Cu_{0.6}Zn_{0.4}Fe_2O_4$	Glass	–	100	$5–15 \times 10^{-3}$	Sultan et al.[100] (2010)
Cation distribution studies					
$ZnFe_2O_4$	Glass	–	100	27	Nakashima et al.[101] (2007)
$NiFe_2O_4$	$MgAl_2O_4$ (001)	58	–	1.65	Klewe et al.[102] (2014)
$Ni_{0.65}Zn_{0.35}Al_{0.8}$ $Fe_{1.2}O_4$	$MgAl_2O_4$ (001)	70	30	3	Lumetzberger et al.[103] (2020)

target of $ZnFe_2O_4$ was prepared by a solid-state reaction method from the starting materials, ZnO and Fe_2O_3. To achieve a highly dense target, this ceramic material was sintered at a high temperature. An appropriate amount of sputter gas (Ar) and reactive gas (O_2) flowed through the sputtering chamber during the time of deposition. The RF reactive sputtering method was used to grow $CoFe_2O_4$ films on $MgAl_2O_4$ (110) and MgO (001) substrates from an iron-cobalt alloy target.[86–88] Both DC and RF sputtering methods were employed to prepare $CuFe_2O_4$ thin films on glass and quartz substrates from a copper ferrite target.[89–91] A $Mn_{0.6}Zn_{0.4}Fe_2$ alloy target was used to deposit Mn-Zn ferrite thin films on glass substrates using the reactive sputter deposition technique.[92] Various oxygen partial pressure and substrate temperatures have been used during the deposition of Mn-Zn ferrite films. Both $MnFe_2O_4$ and $ZnFe_2O_4$ targets were prepared to grow Mn-Zn ferrite thin films of varying Zn content by an alternate RF sputtering method.[93] This method was used at room temperature for depositing Mn-Zn ferrite thin films on different substrates, including Si (100), MgO (100), and SiO_2/Si (100) from two targets. Other doped ferrite thin films, such as Ni-Zn ferrite,[94–99] and Cu–Zn ferrite,[100] have also been deposited on glass, quartz, Si (100), and Pt substrates using the RF magnetron sputtering method. Among various spinel ferrite thin films, the investigation of cation distribution was carried out on $ZnFe_2O_4$, $NiFe_2O_4$, and Al-Zn-doped $NiFe_2O_4$ thin films deposited by RF and DC magnetron sputtering.[101–103] The cation occupancies of Zn^{2+} and Fe^{3+} ions in a $ZnFe_2O_4$ spinel structure explain the ferrimagnetic nature at room temperature and spin-glass behavior.[101] The ferrimagnetic behavior of $NiFe_2O_4$ thin films is due to the compensation of the magnetic moments of Fe at tetrahedral and octahedral sites, as expected in an inverse spinel structure.[102] The magnetocrystalline anisotropy and the intrinsic magnetic damping in Zn/Al-doped $NiFe_2O_4$ thin films are affected by the cation distribution. The reduction of Ni^{2+} at tetrahedral sites with increasing the Zn content leads to a decrease in anisotropy, coercivity, and damping.[103] A summary of ferrite thin films grown by the DC and RF sputter deposition method is provided in Table VII.

Pulsed Laser Deposition (PLD)

PLD is a physical vapor deposition technique that uses a high-power pulsed laser, an ultra-high vacuum, a target material, and substrates for coating. $MgFe_2O_4$ thin films were coated on $MgAl_2O_4$ (100),[104] $SrTiO_3$ (100),[105] and

Table VIII Ferrite thin films deposited by the pulsed laser deposition method

Thin films prepared	Substrates used	Film thickness (nm)	Substrate temperature (°C)	Target substance distance (cm)	Oxygen partial pressure (mTorr)	References
$NiFe_2O_4$, $MgFe_2O_4$	$MgAl_2O_4$ (100)	47, 50	600, 650	–	50	Ade et al.[104] (2020)
$MgFe_2O_4$	$SrTiO_3$ (100)	350	650	6	5–80	Kim et al.[105] (2010)
$MgFe_2O_4$	α-Al_2O_3 (0001)	90	600	–	–	Gupta et al.[106] (2011)
$CoFe_2O_4$	Quartz	110, 200	350, 450	–	–	Nikam et al.[107] (2020)
$CoFe_2O_4$	MgO (001)	215–230	500	6.5	20	Eskandari et al.[108] (2019)
$CoFe_2O_4$	Si (100), $SrTiO_3$ (100)	5–275	27–497	4	–	Oujja et al.[109] (2018)
$CoFe_2O_4$ $CoFe_{1.8}Gd_{0.2}O_4$	Si (100)	200–320	300	1.6	30	Dascalu et al.[110] (2013)
$ZnFe_2O_4$	$SrTiO_3$ (100)	41	400–600	–	12	Zviagin et al.[111] (2016)
$ZnFe_2O_4$, $MgFe_2O_4$	FTO/quartz, α-Al_2O_3 (0001)	380, 290	400, 500	4	3.75	Henning et al.[112] (2019)
$Ni_{1-x}Cr_xFe_2O_4$	Si (100), Si (111)	70	700	5	–	Panwar et al.[113] (2017)
$Ni_{1-x}Zn_xFe_2O_4$	Al_2O_3	130	650	–	0.1	Raghavender et al.[114] (2015)
$Mn_{1-x}Zn_xFe_2O_4$	SiO_2/Si	50	350–500	–	–	Etoh et al.[115] (2009)
Ni-Mn-Zn ferrite	Si (100)	820–1230	650	4.5	7.5–60	Qian et al.[116] (2014)
$CoFe_{1.8}RE_{0.2}O_4$ (RE = Dy, La, Gd)	Si (100)	300–380	600	2.5	7.5	Dascalu et al.[117] (2013)
$MgAl_{2-x}Fe_xO_4$	$MgAl_2O_4$	11	450	–	10	Wisser et al.[118] (2020)
Cation distribution studies						
$CuFe_2O_4$	MgO (100)	100	700	–	1–120	Yang et al.[119] (2005)
$ZnFe_2O_4$	$SrTiO_3$ (100)	70	300	–	0.05–12	Zviagin et al.[120] (2020)
$ZnFe_2O_4$	MgO (100)	17–57	500	–	0.07–75	Torres et al.[121] (2011)
$NiFe_2O_4$	Si (100)	1000	400	–	0.001	Jaffari et al.[122] (2012)

α-Al_2O_3 (0001)[106] substrates using the PLD method. A solid-state reaction method was employed to prepare a dense $MgFe_2O_4$ ceramic target by sintering at high temperatures. In this method, a KrF excimer laser of wavelength 248 nm was used for film deposition with an energy density of 1.2 J/cm^2 and a repetition rate of 10 Hz. The energy density and the pulse frequency of the laser can be varied, based on their requirements. Thin-film growth depends on various parameters, such as substrate temperature, target–substrate distance, and oxygen partial pressure into the chamber. Kim et al.[105] found a decrease in the lattice constant of $MgFe_2O_4$ thin films with increasing the partial pressure of oxygen. $CoFe_2O_4$ thin films have been grown by the PLD technique on various substrates, such as quartz,[107] MgO (001),[108] $SrTiO_3$ (100),[109] and Si (100).[110] A third harmonic Nd:YAG laser of wavelength 355 nm with an energy density 2.5 J/cm^2, pulse duration 6 ns, and repetition rate 10 Hz has been used to irradiate a $CoFe_2O_4$ ceramic target.[107] $CoFe_2O_4$ films were deposited by varying the repetition rate (2, 3, 5, 7, and 10 Hz) of the KrF excimer laser.[108] On the other hand, in a Nd:YAG laser, different excitation wavelengths of 213, 532, and 1064 nm with fluence values of 0.8, 2.4, and 4 J/cm^2, respectively, has been applied for ablating the target.[109] Other spinel ferrite $ZnFe_2O_4$,[111,112] and $NiFe_2O_4$[104] thin films have also been prepared by the PLD method. A site-doped spinel ferrites, such as $Ni_{1-x}Cr_xFe_2O_4$,[113] $Ni_{1-x}Zn_xFe_2O_4$,[114] $Mn_{1-x}Zn_xFe_2O_4$,[115] and Ni-Mn-Zn ferrite[116] thin films, were deposited on Si and sapphire substrates from the bulk targets. Fe^{3+} ions were substituted by lanthanide group elements Dy, La, and Gd in $CoFe_2O_4$ spinel ferrite thin films grown by the PLD technique to investigate the changes in structural properties.[117] Epitaxial $MgAl_{2-x}Fe_xO_4$ ($0.8 < x < 0.2$) films were deposited on a single crystal (001) $MgAl_2O_4$ substrate by PLD.[118] Cation distribution of spinel ferrite thin films has been studied on $CuFe_2O_4$,[119] $ZnFe_2O_4$,[120,121] and $NiFe_2O_4$[122] deposited by the PLD method. The cation inversion decreases with increasing the magnetization, which is found to be increased in $CuFe_2O_4$ thin films with increasing the oxygen partial pressure during PLD. Thus, the cation occupancies in ferrite thin films vary with the oxygen partial pressure.[119] The magnetization alters depending on the cation occupancies of Fe at tetrahedral and octahedral sites of $ZnFe_2O_4$ thin films with oxygen partial pressure during PLD and the annealing conditions.[120,121] The cation

Table IX Ferrite thin films grown by the chemical vapor deposition method

Sample name	Substrate used	Substrate temperature (°C)	Sample thickness (nm)	Chamber pressure (Torr)	Carrier gas	References
$ZnFe_2O_4$	Si (100)	400–800	490	0.75	N_2	Peeters et al.[123] (2017)
$NiFe_2O_4$	(100) $MgAl_2O_4$ and MgO	500–800	> 500	12	Ar	Li et al.[124] (2011)
$NiFe_2O_4$	$MgAl_2O_4$ (100)	500–800	780	12	Ar	Li et al.[125] (2012)
$NiFe_2O_4$	(100) $MgAl_2O_4$ and $SrTiO_3$	600	300	12	Ar	Datta et al.[126] (2012)
$NiFe_2O_4$	(001) PZN-PT and PMN-PT	600–700	1500–2000	–	Ar	Li et al.[127] (2011)
$NiFe_2O_4$	Si (100)	500	700	17	Ar	Yang et al.[128] (2014)
$CoFe_2O_4$	$MgAl_2O_4$ (100)	670	1040	1	Ar	Shen et al.[129] (2014)
$CoFe_2O_4$	(100) ZrO_2 (Y_2O_3)	700	300	7.5	–	Telegin et al.[130] (2019)
$Ni_{1-x}Zn_xFe_2O_4$	Si (100)	500	–	–	Ar	Lane et al.[131] (1998)
$Ni_{1-x}Zn_xFe_2O_4$ ($x \sim 0.4$)	MgO (100)	600	600	12	N_2	Itoh et al.[132] (1989)
$Co_{1-x}Zn_xFe_2O_4$ ($0 \leq x \leq 0.5$)	Soda lime glass	400	500	–	N_2	Fujii et al.[133] (1995)

inversion enhances with increasing the oxygen vacancies in $NiFe_2O_4$ thin films originated during PLD.[122] Therefore, this technique is an efficient ferrite thin film deposition method to alter the cation occupancies in ferrite thin films. Various thin film deposition parameters, such as substrate temperature, target-substance distance, and oxygen partial pressure, are tabulated in Table VIII.

Chemical Deposition Method

In the chemical deposition method, spinel ferrite thin films are coated by both the gaseous and liquid phases of the materials.

Gaseous Phase Deposition

The gaseous phase of the materials is used mainly in chemical vapor deposition (CVD) and atomic layer deposition (ALD) techniques. In the CVD method, $ZnFe_2O_4$ thin films were deposited on Si (100) substrates at a substrate temperature in the range of 400–800°C at low chamber pressure.[123] The precursor was heated to 120°C to vaporize the solution, and nitrogen gas was used to deliver the vapor to the substrate. $NiFe_2O_4$ films were deposited on MgO (100),[124] $MgAl_2O_4$ (100),[124,126] $SrTiO_3$ (100),[126] PZT-PT (001),[127] PMN-PT (001),[127] and Si (100)[128] substrates by direct liquid injection CVD and metal–organic CVD. The surface morphology and chemical composition of $NiFe_2O_4$ thin films are controlled by the various parameters (solution injection rate, flow rate of carrier gas, temperature, and pressure) during liquid phase CVD.[124] Substrates were cleaned thoroughly in acetone, ethanol, and isopropanol before being placed into the deposition chamber. Other spinel ferrites, such as $CoFe_2O_4$ thin films[129,130], Ni-Zn ferrite,[131,132] and Co-Zn ferrite[133] films were also grown by a similar technique. A list of different ferrites prepared by CVD techniques with varying parameters is tabulated in Table IX.

The ALD technique has also been used to fabricate various spinel ferrite thin films. $ZnFe_2O_4$ thin films were grown using a sequential deposition of Fe_3O_4 and ZnO films on mono-crystalline Si (001) substrates.[134] Initially, a layer of Fe_3O_4 was deposited at a temperature of 673 K followed by another coating of ZnO layer at 473 K. Finally, Si (001)/Fe_3O_4/ZnO was annealed at 873 K for 1 h in air atmosphere.[134] Air-stable ferrimagnetic oxides $Ni_xFe_{3-x}O_4$ (nickel ferrite) and $Co_xFe_{3-x}O_4$ (cobalt ferrite) were directly prepared using the ALD technique.[135] The stoichiometry and thickness of these thin films grown by ALD are highly controllable. Pure and smooth $CoFe_2O_4$ thin films of thickness 5–25 nm were grown on $SrTiO_3$ (100) and $SrTiO_3$ (110) single crystals by the ALD method.[136] Pham et al.[137] have demonstrated a radical enhanced ALD method to grow $CoFe_2O_4$ thin films on $SrTiO_3$ (001) substrates at 200 ºC temperature. Apart from spinel ferrite, hexagonal orthoferrite h-$ErFeO_3$ thin films were also fabricated on SiO_2/Si substrates by using the ALD technique.[138]

Liquid Phase Deposition

The extensively used ferrite thin film deposition techniques based on liquid-phase precursors are spin-coating and spray pyrolysis. The initial precursor solutions for depositing thin films using these techniques are prepared by the sol–gel and metal–organic chemical methods. The

Table X Ferrite thin films grown by the liquid phase deposition method

Sample name	Substrate used	Sample thickness (nm)	Annealing temperature and duration	Method used	References
$ZnFe_2O_4$	Glass	1000	–	Spray	Wu et al.[139] (2001)
$ZnFe_2O_4$	Pt	450	–	Spray	Sutka et al.[140] (2013)
$CoFe_2O_4$	Si (100)	400	300–700°C (1 h)	Spin	Sun et al.[141] (2012)
$CoFe_2O_4$	MgO (100)	393	550–850°C (1 h)	Spin	Ninomiya et al.[142] (2015)
$NiFe_2O_4$	Si	700	700°C (3 h)	Spin	Verma et al.[143] (2011)
$MnFe_2O_4$	Glass	400	–	Spray	Zate et al.[144] (2016)
$MgFe_2O_4$	Glass	400	400–600°C (2 h)	Spray	Arabi et al.[145] (2013)
$Ni_{0.3}Zn_{0.7}Fe_2O_4$	ITO/glass	285	400–700°C	Spin	Yusuf et al.[146] (2017)
$Ni_xZn_{1-x}Fe_2O_4$	Quartz	–	900°C (5 h)	Spray	Kumbhar et al.[147] (2015)
$Ni_{1-x}Co_xFe_2O_4$	Glass	200	800°C (1 h)	Spin	Tudorache et al.[148] (2013)
$Co_{1-x}Mn_xFe_2O_4$	Quartz	520	900°C (4 h)	Spray	Bagade et al.[149] (2015)
$Ni_{1-x}Cu_xFe_2O_4$	Glass	270	550°C (3 h)	Spray	Chavan et al.[150] (2018)
$Ni_{1-x}Cd_xFe_2O_4$	Glass	–	500°C (4 h)	Spray	Kardile et al.[151] (2020)
$Co_xRE_{1-x}Fe_2O_4$ (RE: Nd, Eu)	Si	350 ± 30	300–650°C (0.5 h)	Spin	Avazpour et al.[152] (2016)
Cation distribution studies					
$Ni_{0.15}Zn_yFe_{2.85-y}O_4$	Glass	500	–	Spin-spray	Harris et al.[153] (1996)
$NiFe_{2-x}Gd_xO_4$	Pt, quartz	380	700°C (1 h)	Spin	Yao et al.[154] (2021)

concentration of the precursors plays a key role in obtaining a film of the desired thickness. Various ferrite thin films, such as $ZnFe_2O_4$,[139,140] $CoFe_2O_4$,[141,142] $NiFe_2O_4$,[143] $MnFe_2O_4$,[144] and $MgFe_2O_4$[145] have been grown by the liquid-phase deposition method. Easy control of chemical compositions in these techniques also encourages fabricating doped ferrite films, such as $Ni_{1-x}Zn_xFe_2O_4$,[146,147] $Ni_{1-x}Co_xFe_2O_4$,[148] $Co_{1-x}Mn_xFe_2O_4$,[149] $Ni_{1-x}Cu_xFe_2O_4$,[150] $Ni_{1-x}Cd_xFe_2O_4$,[151] and $Co_xRE_{1-x}Fe_2O_4$ (RE: Nd, Eu).[152] Another advantage of liquid phase deposition is the flexibility of choosing the substrates, which results in the deposition of thin films on different substrates, like glass,[139] quartz,[147] mono-crystalline Si,[141] Pt,[140] MgO, [142] and ITO/glass[146]. Finally, these films have been dried to remove the solvents and then annealed at high temperatures to obtain crystalline thin films. $Ni_{0.15}Zn_yFe_{2.85-y}O_4$ and $NiFe_{2-x}Gd_xO_4$ ferrite films have been studied to examine the distribution of cations of tetrahedral and octahedral sites.[153,154] In Ni-Zn ferrite, Zn cations occupy only tetrahedral sites, while Ni and Fe cations occupy both the tetrahedral and octahedral sites. Magnetization is shown to be increased with increasing Zn concentration when Ni occupancy increases to 25% at tetrahedral sites. Gd doping in $NiFe_2O_4$ thin film show higher magnetization due to the Gd doping, exchange interaction, and redistribution of cations at octahedral and tetrahedral sites.[154] The ferrite films prepared by the spin-coating and spray pyrolysis methods are listed in Table X.

Other thin-film deposition techniques such as electrochemical deposition[155] and electrospinning[156] can be employed to fabricate ferrite materials.

At the end of the various synthesis techniques described for preparing ferrite nanoparticles and thin films, a summary of the correlation between the synthesis methods and the cation distribution is established. In the case of ferrite nanoparticle synthesis, it has been found that the milling time and annealing temperature can alter the cation ordering in the mechanical milling method. The degree of inversion initially decreases and saturates with increasing the milling time. Sonication time also plays a major role in determining the cation occupancies in ferrite nanoparticles prepared by the ultrasonic method. The annealing temperature during the preparation of ferrite nanoparticles in the sol–gel method varies the cation distribution, resulting in the variation of different physical properties. Therefore, these techniques are efficient in modifying cation occupancies in ferrite nanoparticles. On the other hand, for ferrite thin film fabrication, the cation distribution predominantly depends on the oxygen partial pressure during the thin film growth using the PLD method. Thus, this technique is found to be an efficient method to alter the cation occupancies in ferrite thin films compared to other methods. The annealing temperatures of ferrite thin films always play a significant role in cation distribution.

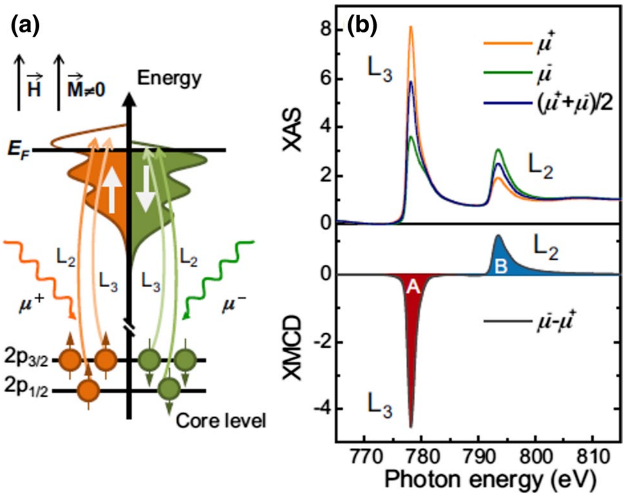

Fig. 5 (a) Schematic of the principle of the XMCD process in a two-step method: (b) XAS and XMCD spectra of the Fe $L_{2,3}$ edge; reprinted from Ref. 157 with permission from Elsevier.

X-ray Magnetic Circular Dichroism (XMCD) on Ferrites

XMCD is a technique that can provide information about cation distribution as well as about the magnetic behavior of ferrite materials. XMCD is the difference between x-ray absorption spectra measured in a magnetic field in presence of left and right circularly polarized light. This method is a well-known and powerful technique to find the atomistic origin of the magnetic moment. Sometimes, these measurements are also performed at cryogenic temperatures. This method is a surface-sensitive element-specific core electron spectroscopy, and is widely used for magnetic studies in material science and inorganic chemistry. Various magnetic systems, such as bulk materials, thin films, multilayers, and nanostructures, can be examined by this technique. It is also used to investigate the phenomena of exchange bias and magnetic anisotropy. XMCD plays a major role in understanding the spin and orbital magnetic moments of 3*d* transition metal, and of lanthanide and actinide systems. XMCD measurement is a two-step process (Fig. 5).[157] At the first step, the angular momentums (ħ and − ħ) of opposite helicity are transferred to the excited photoelectrons by left and right circularly polarized light. Thus, the electrons with opposite spins are mostly excited due to two opposite helicities. The angular momentum of the photon becomes coupled with electron spin through spin–orbit coupling. In the second step, the electrons with spin-up and spin-down create an imbalance in the valence bands in the presence of the magnetic field. These spin-polarized electrons are differently absorbed in valence shells depending on their spin direction. If the valence shell has a net orbital moment, then the magnetization originates from the spin–orbit coupling.

XMCD studies on Ferrite Nanoparticles

Various spinel ferrites have been characterized using XMCD to study the cation distribution and element-specific magnetic moments and hysteresis loops. XAS and XMCD spectra of the Fe $L_{2,3}$ edge collected at 300 K in a magnetic field of 6 T are shown in Fig. 6 for $CoFe_2O_4$ nanoparticles. In the XMCD spectra, three peaks are observed in the Fe L_3 edge. The first negative peak corresponds to the Fe^{2+} at octahedral (O_h) sites, the positive peak represents the Fe^{3+} at the tetrahedral (T_d) sites, and the second negative peak corresponds to Fe^{3+} at octahedral (O_h) sites. The Fe cation distribution at tetrahedral and octahedral sites is found by fitting the experimental spectra using a linear combination of the multiplet ligand field (LFM) calculated spectra for each site. For this simulation, all the parameters are taken from the reported values.[158] Fig. 6c shows the LFM-calculated XMCD spectra for Fe^{2+} O_h, Fe^{3+} T_d, and Fe^{3+} O_h cations. The linear combination of these three spectra fits the experimental curves. The Fe cation distribution for these samples is shown in Table XI. The positive peaks with respect to the negative peak arise due to the antiferromagnetic interaction between the Fe ions at the octahedral and tetrahedral sites.[159] The two positive peaks indicate the ferromagnetic interaction between Fe^{2+} and Fe^{3+} at the octahedral sites.

XMCD studies on the Fe L_3 edge of $Zn_xFe_{3-x}O_4$ nanoparticles demonstrate the amount of ferrous (Fe^{2+}) and ferric (Fe^{3+}) ions oxidation states and their coordination environment.[160] The results show that $Zn_{0.16}$ nanoparticles are more magnetic than Zn_0 with $Zn_{0.92}$, exhibiting lower magnetic moments. Zn^{2+} substituting Fe^{3+} from tetrahedral sites results in an increase in oxidation states from Fe^{2+} to Fe^{3+} at octahedral sites to maintain the charge neutrality of the material. The ratio of Fe^{3+} ions at tetrahedral and octahedral sites has been estimated to be 0.33 in $ZnFe_2O_4$ nanoparticles.[161] In the case of Co-Zn ferrites, Co^{2+} ions prefer to occupy the octahedral sites with a magnetic moment of 3.64 μ_B.[162] The spin and orbital magnetic moments of Fe and Co atoms have been estimated in $Co_xFe_{3-x}O_4$ nanoparticles using XMCD at the temperature of 2 K.[12] The orbital moments of Fe and Co atoms were around 0.05 and 0.15 μ_B respectively. However, the spin magnetic moment is always dominant over the orbital moment for both Fe and Co atoms. The element and site-specific hysteresis loops confirm the improvement of the magnetic order and crystallinity in these materials. The environment of Co^{2+} has been found to be effective in influencing the magnetic anisotropies of $CoFe_2O_4$ nanoparticles.[163]

The orbital magnetic moment of Fe and Cr ions in $Li_{0.5}FeCr_{1.5}O_4$ spinel ferrite was found to be dominant due to the strong spin–orbit coupling and partially filled t_{2g} orbitals.[164] The antiferromagnetically-coupled Fe and

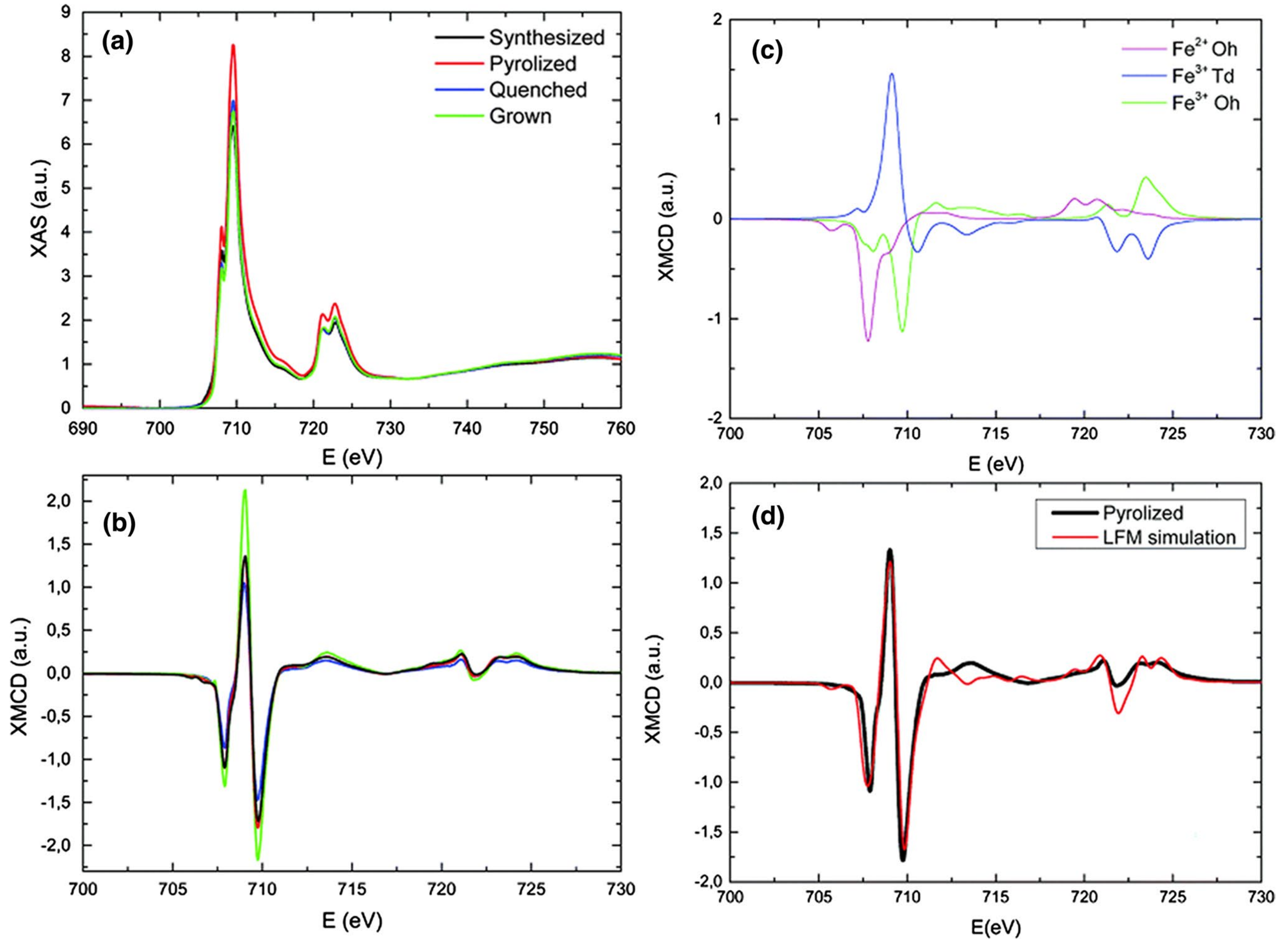

Fig. 6 (a) XAS and (b) XMCD spectra of the Fe $L_{2,3}$ edge for $CoFe_2O_4$ nanoparticles. (c) LFM calculated XMCD spectra and (d) Experimental and simulated spectra; reproduced from Ref. 11 with permission from the Copyright Clearance Center.[11]

Table XI Fe site occupancies in $CoFe_2O_4$ nanoparticles obtained by fitting XMCD spectra using LFM calculations

Samples	Fe^{2+} O_h	Fe^{3+} T_d	Fe^{3+} O_h	Fe^{2+}/Fe^{3+}
Synthesized	0.32	0.75	0.93	0.19
Pyrolized	0.32	0.75	0.93	0.19
Quenched	0.29	0.75	0.96	0.17
Grown	0.29	0.84	0.87	0.18

Cr ions in $Li_{0.5}FeCr_{1.5}O_4$ occupy the tetrahedral and octahedral sites, respectively. XMCD measurements were carried out on $NiFe_{2-x}R_xO_4$ ® = Gd, Dy) nanoparticles to understand the cationic ordering and the element-specific magnetic moment.[165] The spin and orbital moments of the Ni-L, Fe–L, Gd-M, and Dy-M absorption edge with the net magnetic moment of pure and doped $NiFe_2O_4$ have been calculated using the sum rules. Both the spin and orbital magnetic moments were reduced in Gd- and Dy-doped $NiFe_2O_4$ compared to pristine $NiFe_2O_4$. A summary of XMCD measurements on nanoparticles with experimental parameters is listed in Table XII.

XMCD Studies on Ferrite Thin Films

XMCD studies were carried out on ferrite thin films to understand the element-specific magnetic moments with their spin and orbital components. Spinel ferrite $ZnFe_2O_4$ thin films show a ferrimagnetic nature, with the Curie temperature above room temperature, having different cation distribution and oxygen vacancies.[13] Surface magnetic properties and element-specific hysteresis loop were studied in $ZnFe_2O_4$ thin films (Fig. 7).[166] The results show that the Fe^{3+} at octahedral and tetrahedral sites are antiferromagnetically coupled. The magnetic moment of Fe^{3+} at octahedral sites is aligned along the applied magnetic field.

Table XII XMCD measurements carried out on various ferrite nanoparticles at different magnetic fields, and temperatures

Nanoparticles	Magnetic field	Vacuum	Temperature	Spectra at edges	References
$Zn_xFe_{3-x}O_4$	0.6 T	–	Room	Fe $L_{2,3}$, Zn $L_{2,3}$	Byrne et al.[160] (2014)
$ZnFe_2O_4$	0.75 T	10^{-9} torr	300 K	Fe $L_{2,3}$, O K	Singh et al.[161] (2018)
Co-Zn ferrite	4 T	10^{-10} mbar	3 K, 300 K	Fe $L_{2,3}$, Co $L_{2,3}$	Hochepied et al.[162] (2001)
$Co_xFe_{3-x}O_4$	69 kOe	10^{-11} mbar	2 K	Fe $L_{2,3}$, Co $L_{2,3}$	Moya et al.[12] (2021)
$CoFe_2O_4$	6.6 T	10^{-10} mbar	4.2 K	Fe $L_{2,3}$, Co $L_{2,3}$	Daffé et al.[163] (2018)
$CoFe_2O_4$	6 T	–	300 K	Fe $L_{2,3}$, Co $L_{2,3}$	Bartolomé et al.[11] (2016)
$CoFe_2O_4$	3 T	10^{-10} mbar	11 K, 150 K	Fe $L_{2,3}$, Co $L_{2,3}$, O K	Nappini et al.[159] (2015)
$Li_{0.5}FeCr_{1.5}O_4$	200 Oe	3×10^{-10} torr	80–370 K	Fe $L_{2,3}$, Cr $L_{2,3}$	Yang et al.[164] (2020)
$NiFe_{2-x}R_xO_4$ ® = Gd, Dy, Ho)	6 T	–	300 K	Fe $L_{2,3}$, Ni $L_{2,3}$, Gd $M_{4,5}$, Dy $M_{4,5}$	Ugendar et al.[165] (2019)

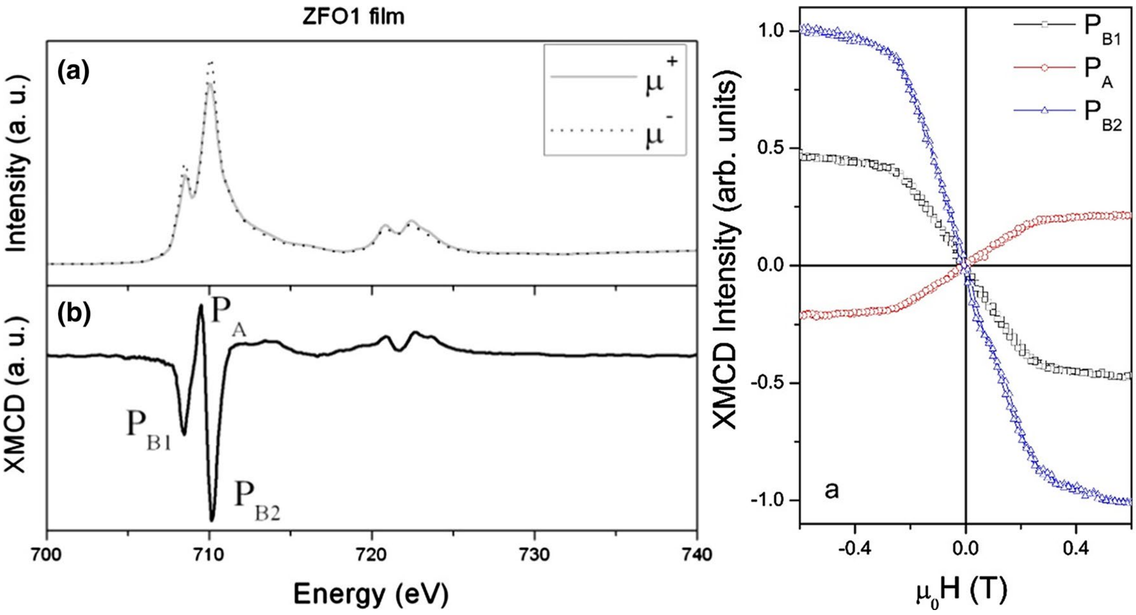

Fig. 7 *Left* XAS and XMCD spectra of the Fe $L_{2,3}$ edge; *right* XMCD hysteresis-loop for $ZnFe_2O_4$ thin films; reprinted from Ref. 166 with permission from Elsevier.[166]

XMCD studies on inverse spinel $NiFe_2O_4$ thin films were carried out to show the cation distribution.[102] Measurements on Fe $L_{2,3}$ edge have revealed the spin magnetic moment of 0.1 μ_B per atom and the ratio of orbital and spin magnetic moment of 0.12. The cation distribution in Fe^{2+} O_h, and Ni^{2+} T_d played an important role in determining the magnetic anisotropy and damping in Zn/Al-doped $NiFe_2O_4$.[103] The XMCD studies at Fe and Mn $L_{2,3}$ edges of $MnFe_2O_4$ (111) thin films confirm the normal spinal structure where tetrahedral sites are occupied by Mn atoms.[167] $MgFe_2O_4$ thin films showed one positive and one negative peak in the Fe $L_{2,3}$ edge XMCD signal.[168] The positive and negative peaks corresponded to the Fe^{3+} ions at the A and B sites, respectively. The role of iron content in magnetic damping of $Mg(Al, Fe)_2O_4$ spinel ferrite thin films was reported by Wisser et al.[118] In this report, the XMCD result confirms the magnetic moment originating predominantly from Fe^{3+} cations distributed at the cathedral and tetrahedral sites with a ratio of 60:40. However, Fe^{2+} cations showed a minimal contribution to the magnetic moment. XMCD studies on $MgAl_{0.5}Fe_{1.5}O_4$ spinel ferrite using total electron yield mode shows peaks at 709.2 eV and 710.0 eV.[169] These peaks indicate the Fe^{3+} is coordinated tetrahedrally and octahedrally, respectively, with a saturation magnetization of 1.5 μ_B per formula unit. However, Fe^{3+} O_h and Fe^{3+} T_d align parallel and antiparallel to the magnetic field, respectively. To find the Fe cation distribution in $Ni_{0.65}Zn_{0.35}Al_{0.8}Fe_{1.2}O_4$ thin films, XMCD spectra on Fe $L_{2,3}$ edge were collected.[170] The weight ratio of the three components associated with Fe^{2+} O_h, Fe^{3+} T_d, and Fe^{3+} O_h cations was 10:46:44. The XMCD

Table XIII XMCD measurements carried out on various spinel ferrite thin films at the different magnetic fields, grazing angles, and temperatures

Thin films	Magnetic field	Grazing angle	Temperature	Spectra at edges	References
$ZnFe_2O_4$	0.6 T	–	Room	Fe $L_{2,3}$	Torres et al.[13] (2014)
$ZnFe_2O_4$	0.6 T	–	Room	Fe $L_{2,3}$	Zélis et al.[166] (2016)
$NiFe_2O_4$	–	–	Room	Fe $L_{2,3}$, Ni $L_{2,3}$	Klewe et al.[102] (2014)
Zn/Al-doped $NiFe_2O_4$	6.8 T	20°	Room	Fe $L_{2,3}$, Ni $L_{2,3}$	Lumetzberger et al.[103] (2020)
$MnFe_2O_4$	5 T	–	300 K	Fe $L_{2,3}$, Mn $L_{2,3}$	Matzen et al.[167] (2011)
$MgFe_2O_4$	0.6 T	-	Room	Fe $L_{2,3}$	Rodríguez et al.[168] (2019)
$Mg(Al, Fe)_2O_4$	400 mT	30°	Room, 30 K	Fe $L_{2,3}$	Wisser et al. [118] (2020)
$MgAl_{0.5}Fe_{1.5}O_4$	0.2 T	30°	Room	Fe $L_{2,3}$	Emori et al.[169] (2018)
$Ni_{0.65}Zn_{0.35}Al_{0.8}Fe_{1.2}O_4$	0.5 T	30°	Room	Fe $L_{2,3}$, Ni $L_{2,3}$	Emori et al.[170] (2017)
$Co_xFe_{3-x}O_4$	4 T	30°	300 K	Fe $L_{2,3}$, Co $L_{2,3}$	Thien et al.[171] (2022)

spectra of the Ni $L_{2,3}$ and Fe $L_{2,3}$ edges confirmed that the moments of the Ni^{2+} O_h, and $Fe^{2+/3+}$ O_h ions were parallel to the applied magnetic field. Using the sum rule, the spin and orbital magnetic moments have been calculated for Co and Fe ions in Co-rich cobalt ferrites.[171] The XMCD results reveal the partial inverse spinal structures in $Co_xFe_{3-x}O_4$ ($x = 1.1, 1.4$) due to the presence of Co^{3+} cations in a low spin state at octahedral B sites. A summary of XMCD measurements on thin films is listed in Table XIII.

Mössbauer Spectroscopy

This technique is widely used to find the cation distribution in ferrites, relying on the radioactive^{57} Fe present in the materials.[57]The Fe nucleus, which emits γ-rays, faces a recoil with an equal and opposite momentum. This is described by the equation,

$$E_{\gamma-ray} = E_{nt} - E_R$$

, where $E_{\gamma\text{-ray}}$ = energy of the γ-ray, E_{nt} = energy of the nuclear transition, and E_R = energy of the recoil. The process when the nucleus absorbs the energy of the γ-ray without recoiling forms the basis of Mössbauer spectroscopy. The Mössbauer effect occurs because of recoil-free absorption. The transmission spectra show isomer shift when the nuclear energy levels of the source and absorber atoms are different. In the case of nuclear quadrupole moment, the transmission spectrum is split into doublets. In the presence of a magnetic field, a sextet pattern appears due to the Zeeman effect. The sextet appears due to 6 nuclear transitions which are allowed by the magnetic dipole selection rule $\Delta m = 0 \pm 1$. The ratio of the relative intensities of these peaks is 3:2:1:1:2:3 for a sample with isotopic magnetic field distribution. Thus, three parameters obtained from these measurements are isomer shift, quadrupole splitting, and hyperfine splitting (Fig. 8).

In the case of ferrites, the double sextet is observed to have Fe at both the tetrahedral and octahedral sites. For example, the general formula of nickel-zinc ferrite is $(Zn^{2}{}_{1-\lambda}Fe^{3+}{}_{\lambda})[Ni^{2+}{}_{\lambda}Fe^{3+}{}_{2-\lambda}]\{O^{2-}\}_4$, where the round and square brackets denote the tetrahedral and octahedral sites, respectively. The degree of inversion, λ, is calculated from the Mössbauer spectral intensities

$$\frac{I_A}{I_B} = \frac{f_A}{f_B}\left\{\frac{\lambda}{2} - \lambda\right\}$$

for bulk and nanosized $Ni_{0.58}Zn_{0.42}Fe_2O_4$,[8] where $\frac{f_A}{f_B} = 1$ at 5 K and $\frac{f_A}{f_B} = 0.94$ at room temperature.[173] The degree of inversion is found to be 0.58 at both low temperature and room temperature. The structure will be normal spinel for $\lambda = 0$ and inverse spinel for $\lambda = 1$. High-energy milling-synthesized $MgFe_2O_4$ nanoparticles exhibit superparamagnetism at low temperatures.[28] The degree of inversion decreases from $\lambda = 0.904(1)$ to $\lambda = 0.856(3)$ and $\lambda = 0.756(1)$ for $MgFe_2O_4$ with increasing milling time of 15 and 30 min, respectively. This result confirms the importance of synthesis parameters on the cation inversion of ferrites. The degree of inversion of bulk and nanosized particles of $CuFe_2O_4$, $MnFe_2O_4$, and $NiFe_2O_4$ show the dependency on particle size distribution. As the particle size decreases, the degree of inversion decreases in $CuFe_2O_4$ and $NiFe_2O_4$, whereas it increases for $MnFe_2O_4$.[15] Mössbauer's studies on $NiFe_{2-x}Cr_xO_4$ ferrite suggest that Cr^{3+} and Ni^{2+} have a strong preference for octahedral sites and Cr^{3+} prefers to substitute Fe^{3+}.[16] So the cation distribution studies on $NiFe_{2-x}Cr_xO_4$ confirm the conversion of inverse spinel to a normal spinel structure by increasing the Cr content in $NiFe_2O_4$. Similar structural changes have been observed in the case of $CoFe_{2-x}Ce_xO_4$ ferrites with increasing the content of Ce.[17] Mössbauer spectroscopy confirms the occupancy of Ni^{2+} at the octahedral sites in solid-state-synthesized $Ni_xMg_{1-x}Fe_2O_4$ ferrite.[174] This reduces the availability of octahedral sites for both Mg^{2+} and Fe^{3+}. So a higher

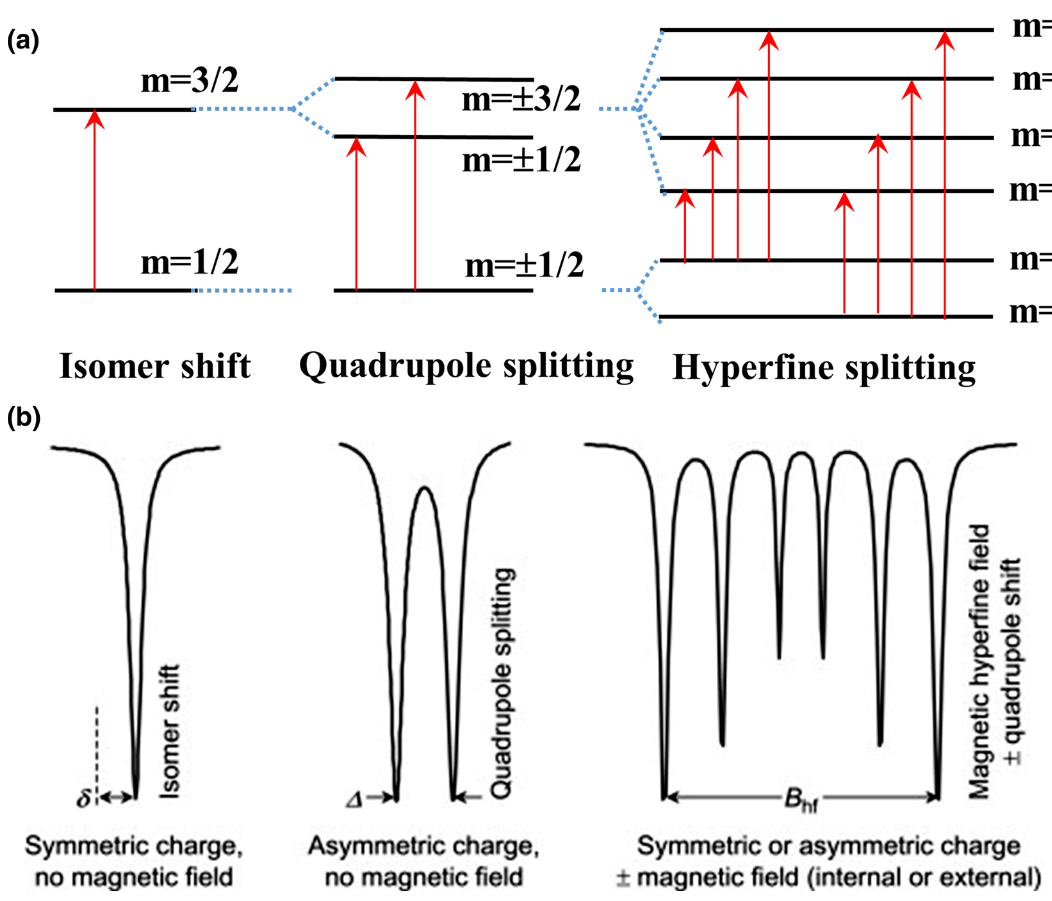

Fig. 8 (a) Nuclear energy levels and the related (b) Mössbauer spectra; reprinted from Ref. 172 with permission from Elsevier[172].

percentage of Mg^{2+} is found at tetrahedral sites for Ni-rich spinel systems. Hence, Mössbauer spectroscopy plays an important role in finding out the cation occupancies at tetrahedral and octahedral sites in a spinel system. However, this method is based on sensing ^{57}Fe which is only 2% of Fe in a system. Thus, the signals that come from the measurements are in most cases low, which is the major drawback of this technique.

X-ray Absorption Spectroscopy (XAS)

The x-ray absorption near-edge structure (XANES) and extended x-ray absorption fine structure (EXAFS) are powerful techniques for studying cation distribution in ferrites.[18,175,176] XANES provides information about the oxidation states and site symmetry of the elements, whereas EXAFS gives information about the coordination number and bond length of the surrounding shells. These techniques are element-selective, and their ability to find the local structure surrounding the selective elements makes them an ideal tool for studying disorder systems. In the case of ferrites, the local structure of both Fe^{3+} and M^{2+} edges can be studied using these techniques. On the other hand, this technique does not provide information regarding the magnetic behavior of the elements.

In the EXAFS signal, the peak observed around 2 Å corresponds to the metal–oxygen bond distance (Fig. 9).[9] On the other hand, the peaks observed between 2.5 and 4 Å correspond to the metal–metal distance, which is crucial for determining the degree of inversion for a spinel ferrite. The distances between two metals having octahedral and tetrahedral sites are approximately 3 and 3.5 Å, respectively. For a normal spinel, M^{2+} ions occupy the tetrahedral site, while, for an inverse spinel, M^{2+} ions occupy the octahedral site. In the case of the M K-edge EXAFS signal, the normal spinel shows a strong peak at 3.5 Å, whereas an inverse spinel shows a strong peak at 3 Å. The peak intensity at 3.5 Å decreases and the peak intensity at 3 Å increases going from a normal spinel to an inverse spinel structure. In the case of Fe K-edge EXAFS signals, the region between 2.5 and 4 Å will be affected similarly to the M K-edge. Although the changes in peak intensities are minimum going from normal spinel to inverse spinel because of the presence of Fe^{3+} at both tetrahedral and octahedral sites. The occupancy of M^{2+} ions at octahedral sites is specified by x_B (M^{2+}), known as

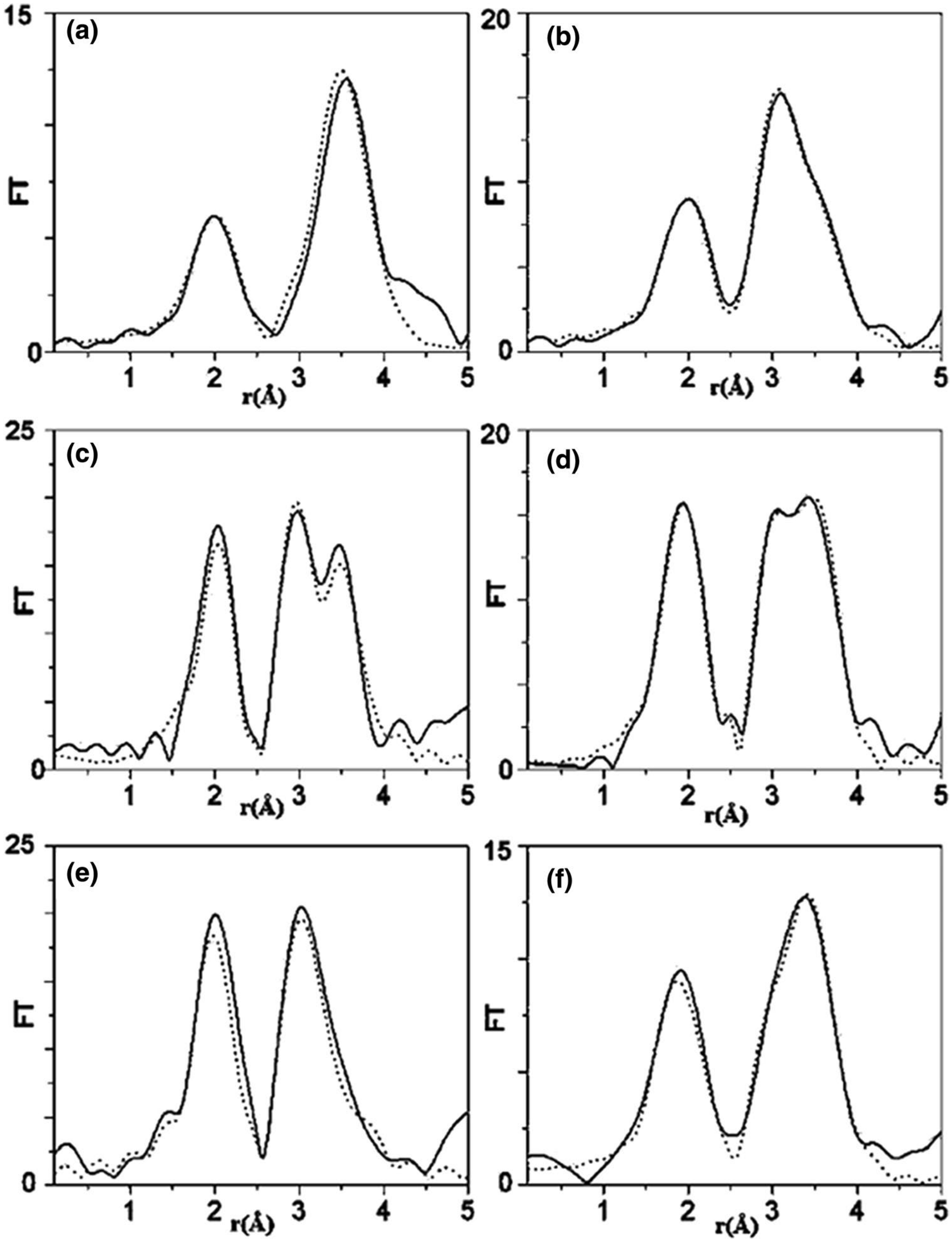

Fig. 9 The modulus of Fourier transforms of the extended x-ray absorption fine structure (EXAFS) signal from (a) Mn, (c) Co, (e) Ni, and (b, d, f) the Fe K-edge for (a, b) $MnFe_2O_4$, (c, d) $CoFe_2O_4$, and (e, f) $NiFe_2O_4$; reprinted from Ref. 9 with permission from the American Chemical Society.[9]

the inversion parameter. Thus, the occupancy of M^{2+} ions at the tetrahedral site is $x_A = 1 - x_B$. Fitting the outer shells of the EXAFS signals with a metal–metal interaction gives information regarding the coordination number and bond distance. The degree of inversion is determined by fitting the EXAFS signals originating due to the tetrahedral and octahedral sites occupied by Fe^{3+} and M^{2+}. In $MnFe_2O_4$, the degree of inversion is found to be 0.2, meaning that 20% of Mn^{2+} occupies the octahedral sites.[19] The degree of inversion in $MnFe_2O_4$ varies with different synthesis methods.[177] It also depends on the particle size distribution, which demonstrates the importance of various synthesis procedures.[20] $CoFe_2O_4$ is a partially inverted spinel ferrite with a degree of inversion from 0.68 to 0.8.[18] $NiFe_2O_4$ is known as an inverted spinel ferrite, whereas $NiFe_2O_4$ nanoparticles prepared by high-energy ball-milling show a mixed spinel structure.[178]

Conclusions

We have demonstrated the role of cation occupancies to define the structure of ferrite materials and their magnetic properties. Since the cation occupancies are predominantly dependent on the synthesis methods, various such methods have been described for preparing ferrite nanoparticles and thin films. The changes of the different physical properties in ferrites with cation occupancies and synthesis methods are also described. A summary between these techniques and the cation distribution in ferrite nanoparticles and thin films is presented. To further study the cation occupancies and magnetic properties of these ferrites, the basic principles and applications of the XMCD technique are illustrated. Other techniques, such as Mössbauer spectroscopy and x-ray absorption spectroscopy, are discussed in order to find the cation distribution in ferrites. The advantages and disadvantages of these techniques are reported, and a comparison is made in determining the cation occupancies.

Conflict of interest The authors declare that they have no conflict of interest.

References

1. T. Kiyomura, Y. Maruo, and M. Gomi, Electrical properties of MgO insulating layers in spin-dependent tunneling junctions using Fe_3O_4. *J. Appl. Phys.* 88, 4768–4771 (2000).
2. X. Sui and M.H. Kryder, Magnetic easy axis randomly in-plane oriented barium hexaferrite thin film media. *Appl. Phys. Lett.* 63, 1582–1584 (1993).
3. B.Y. Wong, X. Sui, D.E. Laughlin, and M.H. Kryder, Microstructural investigations of barium ferrite longitudinal thin-film media. *J. Appl. Phys.* 75, 5966–5968 (1994).
4. A. Lak, S. Disch, and P. Bender, Embracing defects and disorder in magnetic nanoparticles. *Adv. Sci.* 8, 2002682 (2021).
5. X. Zeng, Z. Hou, J. Ju, L. Gao, J. Zhang, and Y. Peng, The cation distributions of Zn-doped normal spinel $MgFe_2O_4$ ferrite and its magnetic properties. *Materials* 15, 2422 (2022).
6. J. Stöhr, H.A. Padmore, S. Anders, T. Stammler, and M.R. Scheinfein, Principles of x-ray magnetic dichroism spectromicroscopy. *Surf. Rev. Lett.* 05, 1297–1308 (1998).
7. T. Abbas, Y. Khan, M. Ahmad, and S. Anwar, X-ray diffraction study of the cation distribution in the Mn-Zn-ferrites. *Solid State Commun.* 82, 701–703 (1992).
8. S. Thakur, S.C. Katyal, A. Gupta, V.R. Reddy, S.K. Sharma, M. Knobel, and M. Singh, Nickel−Zinc ferrite from reverse micelle process: structural and magnetic properties, Mössbauer spectroscopy characterization. *J. Phys. Chem. C* 113, 20785–20794 (2009).
9. D. Carta, M.F. Casula, A. Falqui, D. Loche, G. Mountjoy, C. Sangregorio, and A. Corrias, A structural and magnetic investigation of the inversion degree in ferrite nanocrystals MFe_2O_4 (M = Mn Co, Ni). *J. Phys. Chem. C* 113, 8606–8615 (2009).
10. H. Suzuki, N. Tokitoh, R. Okazaki, S. Nagase, and M. Goto, Synthesis, structure, and reactivity of the first kinetically stabilized silanethione. *J. Am. Chem. Soc.* 120, 11096–11105 (1998).
11. E. Bartolomé, P. Cayado, E. Solano, S. Ricart, J. Gázquez, B. Mundet, M. Coll, T. Puig, X. Obradors, M. Valvidares, J. Herrero-Martín, P. Gargiani, and E. Pellegrin, Magnetic stability against calcining of microwave-synthesized $CoFe_2O_4$ nanoparticles. *New J. Chem.* 40, 6890–6898 (2016).
12. C. Moya, A. Fraile Rodríguez, M. Escoda-Torroella, M. García del Muro, S.R.V. Avula, C. Piamonteze, X. Batlle, and A. Labarta, Crucial role of the Co cations on the destabilization of the ferrimagnetic alignment in Co-ferrite nanoparticles with tunable structural defects. *J. Phys. Chem. C* 125, 691–701 (2021).
13. C.E. Rodríguez Torres, G.A. Pasquevich, P.M. Zélis, F. Golmar, S.P. Heluani, S.K. Nayak, W.A. Adeagbo, W. Hergert, M. Hoffmann, A. Ernst, P. Esquinazi, and S.J. Stewart, Oxygen-vacancy-induced local ferromagnetism as a driving mechanism in enhancing the magnetic response of ferrites. *Phys. Rev. B* 89, 104411 (2014).
14. J.P. Chen, C.M. Sorensen, K.J. Klabunde, G.C. Hadjipanayis, E. Devlin, and A. Kostikas, Size-dependent magnetic properties of $MnFe_2O_4$ fine particles synthesized by coprecipitation. *Phys. Rev. B* 54, 9288–9296 (1996).
15. M. Siddique, and N.M. Butt, Effect of particle size on degree of inversion in ferrites investigated by Mössbauer spectroscopy. *Physica B* 405, 4211–4215 (2010).
16. S.M. Patange, S.E. Shirsath, S.S. Jadhav, and K.M. Jadhav, Cation distribution study of nanocrystalline $NiFe_{2-x}Cr_xO_4$ ferrite by XRD, magnetization and Mössbauer spectroscopy. *Phys. Status Solidi (A)* 209, 347–352 (2012).
17. A. Hashhash, I. Bobrikov, M. Yehia, M. Kaiser, and E. Uyanga, Neutron diffraction and Mössbauer spectroscopy studies for Ce doped $CoFe_2O_4$ nanoparticles. *J. Magn. Magn. Mater.* 503, 166624 (2020).
18. D. Carta, G. Mountjoy, G. Navarra, M.F. Casula, D. Loche, S. Marras, and A. Corrias, X-ray absorption investigation of the formation of Cobalt ferrite nanoparticles in an aerogel silica matrix. *J. Phys. Chem. C* 111, 6308–6317 (2007).
19. F.W. Harrison, W.P. Osmond, and R.W. Teale, Cation distribution and magnetic moment of manganese ferrite. *Phys. Rev.* 106, 865–866 (1957).
20. M.H. Mahmoud, H.H. Hamdeh, A.I. Abdel-Mageed, A.M. Abdallah, and M.K. Fayek, Effect of HEBM on the cation distribution of Mn-ferrite. *Physica B* 291, 49–53 (2000).
21. C. Liu, Y. Li, T. Shi, Q. Peng, and F. Gao, Oxygen defects stabilize the crystal structure of $MgAl_2O_4$ spinel under irradiation. *J. Nucl. Mater.* 527, 151830 (2019).
22. D.S. Mathew, and R.-S. Juang, An overview of the structure and magnetism of spinel ferrite nanoparticles and their synthesis in micro-emulsions. *Chem. Eng. J.* 129, 51–65 (2007).
23. T.F. Marinca, I. Chicinaş, O. Isnard, V. Pop, and F. Popa, Synthesis, structural and magnetic characterization of nanocrystalline nickel ferrite—$NiFe_2O_4$ obtained by reactive milling. *J. Alloy. Compd.* 509, 7931–7936 (2011).
24. T.F. Marinca, I. Chicinaş, and O. Isnard, Synthesis, structural and magnetic characterization of nanocrystalline $CuFe_2O_4$ as obtained by a combined method reactive milling, heat treatment and ball milling. *Ceram. Int.* 38, 1951–1957 (2012).
25. Y. Todaka, M. Nakamura, S. Hattori, K. Tsuchiya, and M. Umemoto, Synthesis of ferrite nanoparticles by mechanochemical processing using a ball mill. *Mater. Trans.* 44, 277–284 (2003).
26. D. Chen, and Y. Zhang, Synthesis of $NiFe_2O_4$ nanoparticles by a low temperature microwave-assisted ball milling technique. *Sci. China Technol. Sci.* 55, 1535–1538 (2012).
27. M.A. Cobos, P. de la Presa, I. Llorente, A. García-Escorial, A. Hernando, and J.A. Jiménez, Effect of preparation methods on magnetic properties of stoichiometric zinc ferrite. *J. Alloy. Compd.* 849, 156353 (2020).
28. V. Šepelák, and K.D. Becker, Comparison of the cation inversion parameter of the nanoscale milled spinel ferrites with that of the quenched bulk materials. *Mater. Sci. Eng., A* 375–377, 861–864 (2004).
29. R.S. Yadav, I. Kuřitka, J. Vilcakova, J. Havlica, L. Kalina, P. Urbánek, M. Machovsky, D. Skoda, M. Masař, and M. Holek,

Sonochemical synthesis of Gd^{3+} doped $CoFe_2O_4$ spinel ferrite nanoparticles and its physical properties. *Ultrason. Sonochem.* 40, 773–783 (2018).

30. R. Singh Yadav, I. Kuřitka, J. Vilcakova, T. Jamatia, M. Machovsky, D. Skoda, P. Urbánek, M. Masař, M. Urbánek, L. Kalina, and J. Havlica, Impact of sonochemical synthesis condition on the structural and physical properties of $MnFe_2O_4$ spinel ferrite nanoparticles. *Ultrason. Sonochem.* 61, 104839 (2020).
31. P.P. Goswami, H.A. Choudhury, S. Chakma, and V.S. Moholkar, Sonochemical synthesis of cobalt ferrite nanoparticles. *Int. J. Chem. Eng.* 2013, 934234 (2013).
32. M. Sivakumar, A. Towata, K. Yasui, T. Tuziuti, T. Kozuka, Y. Iida, M.M. Maiorov, E. Blums, D. Bhattacharya, N. Sivakumar, and M. Ashok, Ultrasonic cavitation induced water in vegetable oil emulsion droplets – a simple and easy technique to synthesize manganese zinc ferrite nanocrystals with improved magnetization. *Ultrason. Sonochem.* 19, 652–658 (2012).
33. A.R. Abbasian, S.S. Hosseini, M. Shayesteh, M. Shafiee, and M. Rafigh Esmaeilzaei, Ultrasonic-assisted solvothermal synthesis of self-assembled copper ferrite nanoparticles. *Int. J. Nano Dimens.* 11, 130–144 (2020).
34. M.A.S. Amulya, H.P. Nagaswarupa, M.R.A. Kumar, C.R. Ravikumar, and K.B. Kusuma, Enhanced photocatalytic and electrochemical properties of Cu doped $NiMnFe_2O_4$ nanoparticles synthesized via probe sonication method. *Appl. Surf. Sci. Adv.* 2, 100038 (2020).
35. P.P. Goswami, H.A. Choudhury, S. Chakma, and V.S. Moholkar, Sonochemical synthesis and characterization of Manganese Ferrite nanoparticles. *Ind. Eng. Chem. Res.* 52, 17848–17855 (2013).
36. H.A. Choudhury, A. Choudhary, M. Sivakumar, and V.S. Moholkar, Mechanistic investigation of the sonochemical synthesis of zinc ferrite. *Ultrason. Sonochem.* 20, 294–302 (2013).
37. Y.X. Gan, A.H. Jayatissa, Z. Yu, X. Chen, and M. Li, Hydrothermal synthesis of nanomaterials. *J. Nanomater.* 2020, 8917013 (2020).
38. D. Ni, Z. Lin, P. Xiaoling, W. Xinqing, and G. Hongliang, Preparation and characterization of Nickel-Zinc Ferrites by a solvothermal method. *Rare Metal Mater. Eng.* 44, 2126–2131 (2015).
39. Z. Li, K. Gao, G. Han, R. Wang, H. Li, X. Zhao, and P. Guo, Solvothermal synthesis of $MnFe_2O_4$ colloidal nanocrystal assemblies and their magnetic and electrocatalytic properties. *New J. Chem.* 39, 361–368 (2015).
40. Y. Yin, W. Liu, N. Huo, and S. Yang, Synthesis of vesicle-like $MgFe_2O_4$/Graphene 3D network anode material with enhanced lithium storage performance. *ACS Sustain. Chem. Eng.* 5, 563–570 (2017).
41. Y. Tang, X. Wang, Q. Zhang, Y. Li, and H. Wang, Solvothermal synthesis of $Co_{1-x}Ni_xFe_2O_4$ nanoparticles and its application in ammonia vapors detection. *Progr. Nat. Sci. Mater. Int.* 22, 53–58 (2012).
42. G. Allaedini, S.M. Tasirin, and P. Aminayi, Magnetic properties of cobalt ferrite synthesized by hydrothermal method. *Int. Nano Lett.* 5, 183–186 (2015).
43. S. Yáñez-Vilar, M. Sánchez-Andújar, C. Gómez-Aguirre, J. Mira, M.A. Señarís-Rodríguez, and S. Castro-García, A simple solvothermal synthesis of MFe_2O_4 (M=Mn, Co and Ni) nanoparticles. *J. Solid State Chem.* 182, 2685–2690 (2009).
44. M. Su, C. He, and K. Shih, Facile synthesis of morphology and size-controlled α-Fe_2O_3 and Fe_3O_4 nano-and microstructures by hydrothermal/solvothermal process: the roles of reaction medium and urea dose. *Ceram. Int.* 42, 14793–14804 (2016).
45. J. Ma, B. Chen, B. Chen, and S. Zhang, Preparation of superparamagnetic ZnFe2O4 submicrospheres via a solvothermal method. *Adv. Nano Res.* 5, 171–178 (2017).
46. T. Yao, Y. Qi, Y. Mei, Y. Yang, R. Aleisa, X. Tong, and J. Wu, One-step preparation of reduced graphene oxide aerogel loaded with mesoporous copper ferrite nanocubes: a highly efficient catalyst in microwave-assisted Fenton reaction. *J. Hazard. Mater.* 378, 120712 (2019).
47. M.A. Aswad, F.A.H. Mutlak, M.S. Jabir, S.K. Abdulridha, A.F. Ahmed, and U.M. Nayef, Laser assisted hydrothermal synthesis of magnetic ferrite nanoparticles for biomedical applications. *J. Phys: Conf. Ser.* 1795, 012030 (2021).
48. B.J. Palla, D. Shah, P.E. Garcia Casillas, and J.A. Matutes-Aquino, Preparation of nanoparticles of barium ferrite from precipitation in micro-emulsions. *J. Nanopart. Res.* 1, 215–221 (1999).
49. Z. Gilani, M. Anjum, M.S. Shifa, H. Ul, H. Asghar, J. Rehman, M. Usmani, S. Aslam, A. Khan, and M. Warsi, Morphological and magnetic behavior of neodymium doped LiNi05Fe2O4 nanocrystalline ferrites prepared via micro-emulsion technique. *Digest J. Nanomater. Biostruct.* 12, 223–228 (2017).
50. K. Pemartin, C. Solans, J. Alvarez-Quintana, and M. Sanchez-Dominguez, Synthesis of Mn–Zn ferrite nanoparticles by the oil-in-water micro-emulsion reaction method. *Colloids Surf., A* 451, 161–171 (2014).
51. R. Ali, M.A. Khan, A. Mahmood, A.H. Chughtai, A. Sultan, M. Shahid, M. Ishaq, and M.F. Warsi, Structural, magnetic and dielectric behavior of $Mg_{1-x}Ca_xNi_yFe_{2-y}O_4$ nano-ferrites synthesized by the micro-emulsion method. *Ceram. Int.* 40, 3841–3846 (2014).
52. R. Ali, M. Azhar Khan, A. Manzoor, M. Shahid, and M. Farooq Warsi, Structural and electromagnetic characterization of Co-Mn doped Ni-Sn ferrites fabricated via micro-emulsion route. *J. Magn. Magn. Mater.* 441, 578–584 (2017).
53. R. Ali, A. Mahmood, M.A. Khan, A.H. Chughtai, M. Shahid, I. Shakir, and M.F. Warsi, Impacts of Ni–Co substitution on the structural, magnetic and dielectric properties of magnesium nano-ferrites fabricated by micro-emulsion method. *J. Alloy. Compd.* 584, 363–368 (2014).
54. M.A. Yousuf, S. Jabeen, M.N. Shahi, M.A. Khan, I. Shakir, and M.F. Warsi, Magnetic and electrical properties of yttrium substituted manganese ferrite nanoparticles prepared via micro-emulsion route. *Res. Phys.* 16, 102973 (2020).
55. M.A. Yousuf, M.M. Baig, M. Waseem, S. Haider, I. Shakir, S. Ud-Din Khan, and M.F. Warsi, Low cost micro-emulsion route synthesis of Cr-substituted $MnFe_2O_4$ nanoparticles. *Ceram. Int.* 45, 22316–22323 (2019).
56. K. Ganure, L. Dhale, V. Tukaram, and K. Lohar, Synthesis and characterization of Lanthanum-doped Ni-Co-Zn spinel ferrites nanoparticles via normal micro-emulsion method. *Int. J. Nanotechnol. Appl.* 11, 189–195 (2017).
57. S. Sagadevan, Z.Z. Chowdhury, and R.F. Rafique, Preparation and characterization of Nickel ferrite nanoparticles via co-precipitation method. *Mater. Res.* 21, e20160533 (2018).
58. Y. Peng, C. Xia, M. Cui, Z. Yao, and X. Yi, Effect of reaction condition on microstructure and properties of $(NiCuZn)Fe_2O_4$ nanoparticles synthesized via co-precipitation with ultrasonic irradiation. *Ultrason. Sonochem.* 71, 105369 (2021).
59. K. Islam, M. Haque, A. Kumar, A. Hoq, F. Hyder, and S.M. Hoque, Manganese ferrite nanoparticles ($MnFe_2O_4$): Size dependence for hyperthermia and negative/positive contrast enhancement in MRI. *Nanomaterials* 10, 2297 (2020).
60. M.S.A. Darwish, H. Kim, H. Lee, C. Ryu, J.Y. Lee, and J. Yoon, Synthesis of magnetic ferrite nanoparticles with high hyperthermia performance via a controlled co-precipitation method. *Nanomaterials* 9, 1176 (2019).
61. H. El Moussaoui, T. Mahfoud, S. Habouti, K. El Maalam, M. Ben Ali, M. Hamedoun, O. Mounkachi, R. Masrour, E.K. Hlil, and

A. Benyoussef, Synthesis and magnetic properties of tin spinel ferrites doped manganese. *J. Magn. Magn. Mater.* 405, 181–186 (2016).

62. R.T. Olsson, G. Salazar-Alvarez, M.S. Hedenqvist, U.W. Gedde, F. Lindberg, and S.J. Savage, Controlled synthesis of near-stoichiometric cobalt ferrite nanoparticles. *Chem. Mater.* 17, 5109–5118 (2005).
63. C. Pereira, A.M. Pereira, C. Fernandes, M. Rocha, R. Mendes, M.P. Fernández-García, A. Guedes, P.B. Tavares, J.-M. Grenèche, J.P. Araújo, and C. Freire, Superparamagnetic MFe2O4 (M = Fe Co, Mn) nanoparticles: Tuning the particle size and magnetic properties through a novel one-step coprecipitation route. *Chem. Mater.* 24, 1496–1504 (2012).
64. A. Tadjarodi, M. Imani, and M. Salehi, $ZnFe_2O_4$ nanoparticles and a clay encapsulated $ZnFe_2O_4$ nanocomposite: synthesis strategy, structural characteristics and the adsorption of dye pollutants in water. *RSC Adv.* 5, 56145–56156 (2015).
65. S.K. Jesudoss, J.J. Vijaya, L.J. Kennedy, P.I. Rajan, H.A. Al-Lohedan, R.J. Ramalingam, K. Kaviyarasu, and M. Bououdina, Studies on the efficient dual performance of $Mn_{1-x}Ni_xFe_2O_4$ spinel nanoparticles in photodegradation and antibacterial activity. *J. Photochem. Photobiol. B* 165, 121–132 (2016).
66. M. Venkatesh, G.S. Kumar, S. Viji, S. Karthi, and E.K. Girija, Microwave assisted combustion synthesis and characterization of nickel ferrite nanoplatelets. *Modern Electron. Mater.* 2, 74–78 (2016).
67. Kozakova, Z.; Kuřitka, I.; Bazant, P.; Machovsky, M.; Pastorek, M.; Babayan, V.; Ltd, T, Simple and effective preparation of cobalt ferrite nanoparticles by microwave-assisted solvothermal method. In: Nanocon 2012, 4th international conference, Brno, Czech Republic, EU, 01/01; Brno, Czech Republic, EU, 2012; pp 763-766
68. M. Giridhar, H.S.B. Naik, C.N. Sudhamani, M.C. Prabakara, R. Kenchappa, N. Venugopal, and S. Patil, Microwave-assisted synthesis of water-soluble styrylpyridine dye-capped zinc oxide nanoparticles for antibacterial applications. *J. Chin. Chem. Soc.* 67, 316–323 (2020).
69. S.-H. Yu, Q.-L. Wang, Y. Chen, Y. Wang, and J.-H. Wang, Microwave-assisted synthesis of spinel ferrite nanospherolites. *Mater. Lett.* 278, 128431 (2020).
70. S. Shirsath, D. Wang, S. Jadhav, M. Mane, and S. Li, Ferrites obtained by sol-gel method, *Handbook of Sol-Gel Science and Technology*. ed. L. Klein, M. Aparicio, and A. Jitianu (Cham: Springer, 2018), pp. 695–735.
71. L. Zhang, and Y. Wu, Sol-gel synthesized magnetic $MnFe_2O_4$ spinel ferrite nanoparticles as novel catalyst for oxidative degradation of methyl orange. *J. Nanomater.* 2013, 640940 (2013).
72. A. Gatelytė, D. Jasaitis, A. Beganskienė, and A. Kareiva, Sol-gel synthesis and characterization of selected transition metal nano-ferrites. *Mater. Sci.* (2011). https://doi.org/10.5755/j01.ms.17.3.598.
73. S.A. Rashdan, and L.J. Hazeem, Synthesis of spinel ferrites nanoparticles and investigating their effect on the growth of microalgae Picochlorum sp. *Arab. J. Basic Appl. Sci.* 27, 134–141 (2020).
74. R.S. Yadav, I. Kuřitka, J. Vilcakova, J. Havlica, J. Masilko, L. Kalina, J. Tkacz, V. Enev, and M. Hajdúchová, Structural, magnetic, dielectric, and electrical properties of $NiFe_2O_4$ spinel ferrite nanoparticles prepared by honey-mediated sol-gel combustion. *J. Phys. Chem. Solids* 107, 150–161 (2017).
75. R.S. Yadav, I. Kuřitka, J. Vilcakova, P. Urbánek, M. Machovsky, M. Masař, and M. Holek, Structural, magnetic, optical, dielectric, electrical and modulus spectroscopic characteristics of $ZnFe_2O_4$ spinel ferrite nanoparticles synthesized via honey-mediated sol-gel combustion method. *J. Phys. Chem. Solids* 110, 87–99 (2017).
76. K. Jalaiah, and K. Vijaya Babu, Structural, magnetic and electrical properties of nickel doped Mn-Zn spinel ferrite synthesized by sol-gel method. *J. Magn. Magn. Mater.* 423, 275–280 (2017).
77. R.S. Yadav, J. Havlica, M. Hnatko, P. Šajgalík, C. Alexander, M. Palou, E. Bartoníčková, M. Boháč, F. Frajkorová, J. Masilko, M. Zmrzlý, L. Kalina, M. Hajdúchová, and V. Enev, Magnetic properties of $Co_{1-x}Zn_xFe_2O_4$ spinel ferrite nanoparticles synthesized by starch-assisted sol–gel autocombustion method and its ball milling. *J. Magn. Magn. Mater.* 378, 190–199 (2015).
78. D.H. Bobade, S.M. Rathod, and M.L. Mane, Sol–gel auto-combustion synthesis, structural and enhanced magnetic properties of Ni^{2+} substituted nanocrystalline Mg–Zn spinel ferrite. *Physica B* 407, 3700–3704 (2012).
79. K.M. Muniba, A.D. Chandio, M.S. Akhtar, J.K. Khan, G. Mustafa, N.U. Channa, Z.A. Gilani, and H.M. Asghar, Aluminum substitution in Ni-Co based spinel ferrite nanoparticles by sol–gel auto-combustion method. *J. Electron. Mater.* 50, 3302–3311 (2021).
80. S. Jauhar, J. Kaur, A. Goyal, and S. Singhal, Tuning the properties of cobalt ferrite: a road towards diverse applications. *RSC Adv.* 6, 97694–97719 (2016).
81. M. Gu, B. Yue, R. Bao, and H. He, Template synthesis of magnetic one-dimensional nanostructured spinel MFe_2O_4 (M=Ni, Mg, Co). *Mater. Res. Bull.* 44, 1422–1427 (2009).
82. M. Sultan, and R. Singh, Magnetic and optical properties of rf-sputtered zinc ferrite thin films. *J. Appl. Phys.* 105, 07A512 (2009).
83. Y.-C. Liang, and H.-Y. Hsia, Growth and crystallographic feature-dependent characterization of spinel zinc ferrite thin films by RF sputtering. *Nanoscale Res. Lett.* 8, 537 (2013).
84. S. Nakashima, K. Fujita, K. Tanaka, and K. Hirao, High magnetization and the high-temperature superparamagnetic transition with intercluster interaction in disordered zinc ferrite thin film. *J. Phys.: Condens. Matter* 17, 137–149 (2004).
85. M. Bohra, S. Prasad, N. Kumar, D.S. Misra, S.C. Sahoo, N. Venkataramani, and R. Krishnan, Large room temperature magnetization in nanocrystalline zinc ferrite thin films. *Appl. Phys. Lett.* 88, 262506 (2006).
86. T. Niizeki, T. Kikkawa, K.-I. Uchida, M. Oka, K.Z. Suzuki, H. Yanagihara, E. Kita, and E. Saitoh, Observation of longitudinal spin-Seebeck effect in cobalt-ferrite epitaxial thin films. *AIP Adv.* 5, 053603 (2015).
87. H. Yanagihara, Y. Utsumi, T. Niizeki, J. Inoue, and E. Kita, Perpendicular magnetic anisotropy in epitaxially strained cobalt-ferrite (001) thin films. *J. Appl. Phys.* 115, 17A719 (2014).
88. T. Niizeki, Y. Utsumi, R. Aoyama, H. Yanagihara, J.-I. Inoue, Y. Yamasaki, H. Nakao, K. Koike, and E. Kita, Extraordinarily large perpendicular magnetic anisotropy in epitaxially strained cobalt-ferrite CoxFe3−xO4 (001) (x = 0.75, 1.0) thin films. *Appl. Phys. Lett.* 103, 162407 (2013).
89. M.A. Haija, A.I. Ayesh, S. Ahmed, and M.S. Katsiotis, Selective hydrogen gas sensor using $CuFe_2O_4$ nanoparticle based thin film. *Appl. Surf. Sci.* 369, 443–447 (2016).
90. M. Desai, S. Prasad, N. Venkataramani, I. Samajdar, A.K. Nigam, and R. Krishnan, Cubic phase stabilization in sputter-deposited nanocrystalline copper ferrite thin films with large magnetization. *IEEE Trans. Magn.* 38, 3012–3014 (2002).
91. Š Višňovský, M. Veis, E. Lišková, V. Kolinský, P.D. Kulkarni, N. Venkataramani, P. Shiva, and R. Krishnan, MOKE spectroscopy of sputter-deposited Cu-ferrite films. *J. Magn. Magn. Mater.* 290–291, 195–197 (2005).
92. S. Nakagawa, S. Saito, T. Kamiki, and S.-H. Kong, Mn–Zn spinel ferrite thin films prepared by high rate reactive facing targets sputtering. *J. Appl. Phys.* 93, 7996–7998 (2003).

93. L. Wang, J. Bai, Z. Li, J. Cao, F. Wei, and Z. Yang, The influence of substrate on the magnetic properties of MnZn ferrite thin film fabricated by alternate sputtering. *Phys. Status Solidi (A)* 205, 2453–2457 (2008).
94. L. Jang-Sik, L. Byung-Il, and J. Seung-Ki, Effects of process parameters on structure and magnetic properties of sputtered Ni-Zn ferrite thin films. *IEEE Trans. Magn.* 35, 3415–3417 (1999).
95. M.R. Koblischka, M. Kirsch, M. Brust, A. Koblischka-Veneva, and U. Hartmann, Preparation of thin ferrite films on silicon using RF sputtering. *Phys. Status Solidi (A)* 205, 1783–1786 (2008).
96. M. Desai, S. Prasad, N. Venkataramani, I. Samajdar, A.K. Nigam, N. Keller, R. Krishnan, E.M. Baggio-Saitovitch, B.R. Pujada, and A. Rossi, Anomalous variation of coercivity with annealing in nanocrystalline NiZn ferrite films. *J. Appl. Phys.* 91, 7592–7594 (2002).
97. D. Guo, Z. Zhang, M. Lin, X. Fan, G. Chai, Y. Xu, and D. Xue, Ni–Zn ferrite films with high resonance frequency in the gigahertz range deposited by magnetron sputtering at room temperature. *J. Phys. D Appl. Phys.* 42, 125006 (2009).
98. D. Guo, X. Fan, G. Chai, C. Jiang, X. Li, and D. Xue, Structural and magnetic properties of NiZn ferrite films with high saturation magnetization deposited by magnetron sputtering. *Appl. Surf. Sci.* 256, 2319–2322 (2010).
99. L. Wu, C. Dong, X. Wang, J. Li, and M. Li, Annealing effect on the bipolar resistive switching memory of NiZn ferrite films. *J. Alloy. Compd.* 779, 794–799 (2019).
100. M. Sultan, and R. Singh, Crystal structure and magnetic properties of rf-sputtered Cu–Zn ferrite thin films. *J. Appl. Phys.* 107, 09A510 (2010).
101. S. Nakashima, K. Fujita, K. Tanaka, K. Hirao, T. Yamamoto, and I. Tanaka, First-principles XANES simulations of spinel zinc ferrite with a disordered cation distribution. *Phys. Rev. B* 75, 174443 (2007).
102. C. Klewe, M. Meinert, A. Boehnke, K. Kuepper, E. Arenholz, A. Gupta, J.-M. Schmalhorst, T. Kuschel, and G. Reiss, Physical characteristics and cation distribution of $NiFe_2O_4$ thin films with high resistivity prepared by reactive co-sputtering. *J. Appl. Phys.* 115, 123903 (2014).
103. J. Lumetzberger, M. Buchner, S. Pile, V. Ney, W. Gaderbauer, N. Daffé, M.V. Moro, D. Primetzhofer, K. Lenz, and A. Ney, Influence of structure and cation distribution on magnetic anisotropy and damping in Zn/Al doped nickel ferrites. *Phys. Rev. B* 102, 054402 (2020).
104. R. Ade, Y.S. Chen, and J.G. Lin, Effect of atomic replacement on the magnetic anisotropy in epitaxially grown ferrite thin films. *J. Magn. Magn. Mater.* 496, 165956 (2020).
105. K.S. Kim, P. Muralidharan, S.H. Han, J.S. Kim, H.G. Kim, and C.I. Cheon, Influence of oxygen partial pressure on the epitaxial $MgFe_2O_4$ thin films deposited on $SrTiO_3$ (100) substrate. *J. Alloy. Compd.* 503, 460–463 (2010).
106. R.K. Gupta, and F. Yakuphanoglu, Epitaxial growth of $MgFe_2O_4$ (111) thin films on sapphire (0001) substrate. *Mater. Lett.* 65, 3058–3060 (2011).
107. S.M. Nikam, A. Sharma, M. Rahaman, A.M. Teli, S.H. Mujawar, D.R.T. Zahn, P.S. Patil, S.C. Sahoo, G. Salvan, and P.B. Patil, Pulsed laser deposited $CoFe_2O_4$ thin films as supercapacitor electrodes. *RSC Adv.* 10, 19353–19359 (2020).
108. F. Eskandari, P. Kameli, and H. Salamati, Effect of laser pulse repetition rate on morphology and magnetic properties of cobalt ferrite films grown by pulsed laser deposition. *Appl. Surf. Sci.* 466, 215–223 (2019).
109. M. Oujja, L. Martín-García, E. Rebollar, A. Quesada, M.A. García, J.F. Fernández, J.F. Marco, J. de la Figuera, and M. Castillejo, Effect of wavelength, deposition temperature and substrate type on cobalt ferrite thin films grown by pulsed laser deposition. *Appl. Surf. Sci.* 452, 19–31 (2018).
110. G. Dascalu, G. Pompilian, B. Chazallon, O.F. Caltun, S. Gurlui, and C. Focsa, Femtosecond pulsed laser deposition of cobalt ferrite thin films. *Appl. Surf. Sci.* 278, 38–42 (2013).
111. V. Zviagin, Y. Kumar, I. Lorite, P. Esquinazi, M. Grundmann, and R. Schmidt-Grund, Ellipsometric investigation of $ZnFe_2O_4$ thin films in relation to magnetic properties. *Appl. Phys. Lett.* 108, 131901 (2016).
112. R.A. Henning, P. Uredat, C. Simon, A. Bloesser, P. Cop, M.T. Elm, and R. Marschall, Characterization of MFe_2O_4 (M = Mg, Zn) thin films prepared by pulsed laser deposition for photoelectrochemical applications. *J. Phys. Chem. C* 123, 18240–18247 (2019).
113. K. Panwar, S. Tiwari, K. Bapna, N.L. Heda, R.J. Choudhary, D.M. Phase, and B.L. Ahuja, The effect of Cr substitution on the structural, electronic and magnetic properties of pulsed laser deposited $NiFe_2O_4$ thin films. *J. Magn. Magn. Mater.* 421, 25–30 (2017).
114. A.T. Raghavender, N. Hoa Hong, E. Chikoidze, Y. Dumont, and M. Kurisu, Effect of zinc doping on the structural and magnetic properties of nickel ferrite thin films fabricated by pulsed laser deposition technique. *J. Magn. Magn. Mater.* 378, 358–361 (2015).
115. H. Etoh, J. Sato, Y. Murakami, A. Takahashi, and R. Nakatani, Magnetic properties of Mn-Zn ferrite thin films fabricated by pulsed laser deposition. *J. Phys: Conf. Ser.* 165, 012031 (2009).
116. Y.W. Qian, J.X. Deng, H. Zheng, P. Zheng, L. Zheng, and H.B. Qin, Influence of oxygen pressure on the properties of Ni-Mn-Zn ferrite films on silicon substrate. *J. Electron. Mater.* 43, 4289–4293 (2014).
117. G. Dascalu, G. Pompilian, B. Chazallon, V. Nica, O.F. Caltun, S. Gurlui, and C. Focsa, Rare earth doped cobalt ferrite thin films deposited by PLD. *Appl. Phys. A* 110, 915–922 (2013).
118. J.J. Wisser, L.J. Riddiford, A. Altman, P. Li, S. Emori, P. Shafer, C. Klewe, A.T. N'Diaye, E. Arenholz, and Y. Suzuki, The role of iron in magnetic damping of Mg(Al, Fe)2_O4 spinel ferrite thin films. *Appl. Phys. Lett.* 116, 142406 (2020).
119. A. Yang, Z. Chen, X. Zuo, D. Arena, J. Kirkland, C. Vittoria, and V.G. Harris, Cation-disorder-enhanced magnetization in pulsed-laser-deposited $CuFe_2O_4$ films. *Appl. Phys. Lett.* 86, 252510 (2005).
120. V. Zviagin, C. Sturm, P.D. Esquinazi, M. Grundmann, and R. Schmidt-Grund, Control of magnetic properties in spinel $ZnFe_2O_4$ thin films through intrinsic defect manipulation. *J. Appl. Phys.* 128, 165702 (2020).
121. C.E. Rodríguez Torres, F. Golmar, M. Ziese, P. Esquinazi, and S.P. Heluani, Evidence of defect-induced ferromagnetism in $ZnFe_2O_4$ thin films. *Phys. Rev. B* 84, 064404 (2011).
122. G.H. Jaffari, A.K. Rumaiz, J.C. Woicik, and S.I. Shah, Influence of oxygen vacancies on the electronic structure and magnetic properties of $NiFe_2O_4$ thin films. *J. Appl. Phys.* 111, 093906 (2012).
123. D. Peeters, D.H. Taffa, M.M. Kerrigan, A. Ney, N. Jöns, D. Rogalla, S. Cwik, H.-W. Becker, M. Grafen, A. Ostendorf, C.H. Winter, S. Chakraborty, M. Wark, and A. Devi, Photoactive zinc ferrites fabricated via conventional CVD approach. *ACS Sustain. Chem. Eng.* 5, 2917–2926 (2017).
124. N. Li, Y.-H.A. Wang, M.N. Iliev, T.M. Klein, and A. Gupta, Growth of atomically smooth epitaxial nickel ferrite films by direct liquid injection CVD. *Chem. Vap. Depos.* 17, 261–269 (2011).
125. N. Li, S. Schäfer, R. Datta, T. Mewes, T.M. Klein, and A. Gupta, Microstructural and ferromagnetic resonance properties of

epitaxial nickel ferrite films grown by chemical vapor deposition. *Appl. Phys. Lett.* 101, 132409 (2012).

126. R. Datta, B. Loukya, N. Li, and A. Gupta, Structural features of epitaxial $NiFe_2O_4$ thin films grown on different substrates by direct liquid injection chemical vapor deposition. *J. Cryst. Growth* 345, 44–50 (2012).
127. N. Li, M. Liu, Z. Zhou, N.X. Sun, D.V.B. Murthy, G. Srinivasan, T.M. Klein, V.M. Petrov, and A. Gupta, Electrostatic tuning of ferromagnetic resonance and magnetoelectric interactions in ferrite-piezoelectric heterostructures grown by chemical vapor deposition. *Appl. Phys. Lett.* 99, 192502 (2011).
128. Y. Yang, Q. Tao, G. Srinivasan, and C.G. Takoudis, Cyclic chemical vapor deposition of nickel ferrite thin films using organometallic precursor combination. *ECS J. Solid State Sci. Technol.* 3, P345–P352 (2014).
129. L. Shen, M. Althammer, N. Pachauri, B. Loukya, R. Datta, M. Iliev, N. Bao, and A. Gupta, Epitaxial growth of spinel cobalt ferrite films on $MgAl_2O_4$ substrates by direct liquid injection chemical vapor deposition. *J. Cryst. Growth* 390, 61–66 (2014).
130. A.V. Telegin, I.D. Lobov, I.E. Korsakov, V.A. Bessonova, and Y.P. Sukhorukov, Magnetooptical properties of epitaxial strained ferrite films grown by MOCVD method. *J. Phys: Conf. Ser.* 1389, 012107 (2019).
131. P.A. Lane, P.J. Wright, M.J. Crosbie, A.D. Pitt, C.L. Reeves, B. Cockayne, A.C. Jones, and T.J. Leedham, Liquid injection metal organic chemical vapour deposition of nickel zinc ferrite thin films. *J. Cryst. Growth* 192, 423–429 (1998).
132. H. Itoh, T. Uemura, H. Yamaguchi, and S. Naka, Chemical vapour deposition of epitaxial Ni-Zn ferrite films by thermal decomposition of acetylacetonato complexes. *J. Mater. Sci.* 24, 3549–3552 (1989).
133. E. Fujii, H. Torii, R. Takayama, and T. Hirao, Preparation of Co Ferrite Films by Plasma-Enhanced Metalorganic Chemical Vapor Deposition. *Japn. J. Appl. Phys.* 34, 130–131 (1995).
134. Y. Zhang, W. Ren, G. Niu, C. Li, C. Wang, Z.-D. Jiang, M. Liu, and Z.-G. Ye, Atomic layer deposition of void-free $ZnFe_2O_4$ thin films and their magnetic properties. *Thin Solid Films* 709, 138206 (2020).
135. Y.T. Chong, E.M.Y. Yau, K. Nielsch, and J. Bachmann, Direct atomic layer deposition of ternary ferrites with various magnetic properties. *Chem. Mater.* 22, 6506–6508 (2010).
136. M. Coll, J.M. Montero Moreno, J. Gazquez, K. Nielsch, X. Obradors, and T. Puig, Low temperature stabilization of nanoscale epitaxial spinel ferrite thin films by atomic layer deposition. *Adv. Func. Mater.* 24, 5368–5374 (2014).
137. C.D. Pham, J. Chang, M.A. Zurbuchen, and J.P. Chang, Magnetic properties of $CoFe_2O_4$ thin films synthesized by radical-enhanced atomic layer deposition. *ACS Appl. Mater. Interfaces.* 9, 36980–36988 (2017).
138. S. Vangelista, A. Lamperti, C. Wiemer, M. Fanciulli, and R. Mantovan, Atomic layer deposition of hexagonal $ErFeO_3$ thin films on SiO_2/Si. *Thin Solid Films* 604, 18–22 (2016).
139. Z. Wu, M. Okuya, and S. Kaneko, Spray pyrolysis deposition of zinc ferrite films from metal nitrates solutions. *Thin Solid Films* 385, 109–114 (2001).
140. A. Sutka, J. Zavickis, G. Mezinskis, D. Jakovlevs, and J. Barloti, Ethanol monitoring by $ZnFe_2O_4$ thin film obtained by spray pyrolysis. *Sens. Actuators B Chem.* 176, 330–334 (2013).
141. J. Sun, Z. Wang, Y. Wang, Y. Zhu, T. Shen, L. Pang, K. Wei, and F. Li, Synthesis of the nanocrystalline $CoFe_2O_4$ ferrite thin films by a novel sol–gel method using glucose as an additional agent. *Mater. Sci. Eng., B* 177, 269–273 (2012).
142. M. Ninomiya, M. Sasaki, T. Tsurui, K. Shinozaki, T. Komatsu, and T. Ishibashi, Preparation and characterization of Co ferrite thin films on MgO (100) substrates by metal organic decomposition. *Sens. Mater.* 27, 925–931 (2015).
143. K. Chand Verma, V. Pratap Singh, M. Ram, J. Shah, and R.K. Kotnala, Structural, microstructural and magnetic properties of $NiFe_2O_4$, $CoFe_2O_4$ and $MnFe_2O_4$ nanoferrite thin films. *J. Magn. Magn. Mater.* 323, 3271–3275 (2011).
144. M.K. Zate, V.V. Jadhav, S.K. Gore, J.H. Shendkar, S.U. Ekar, A. Al-Osta, M. Naushad, and R.S. Mane, Structural, morphological and electrochemical supercapacitive properties of sprayed manganese ferrite thin film electrode. *J. Anal. Appl. Pyrol.* 122, 224–229 (2016).
145. H. Arabi, and N. Khalili Moghadam, Nanostructure and magnetic properties of magnesium ferrite thin films deposited on glass substrate by spray pyrolysis. *J. Magn. Magn. Mater.* 335, 144–148 (2013).
146. Y. Yusuf, R.A.S. Azis, S. Kanagesan, and G. Bahmanrokh, Microstructure and magnetic properties of Ni-Zn ferrite thin film synthesized using sol-gel and spin-coating technique. *J. Aus. Ceram. Soc.* 53, 767–774 (2017).
147. S.S. Kumbhar, M.A. Mahadik, V.S. Mohite, Y.M. Hunge, K.Y. Rajpure, and C.H. Bhosale, Effect of Ni content on the structural, morphological and magnetic properties of spray deposited Ni–Zn ferrite thin films. *Mater. Res. Bull.* 67, 47–54 (2015).
148. F. Tudorache, P.D. Popa, M. Dobromir, and F. Iacomi, Studies on the structure and gas sensing properties of nickel–cobalt ferrite thin films prepared by spin coating. *Mater. Sci. Eng., B* 178, 1334–1338 (2013).
149. A.A. Bagade, and K.Y. Rajpure, Studies on NO2 gas sensing properties of sprayed Co1−xMnxFe2O4 (0≤x≤0.5) spinel ferrite thin films. *Ceram. Int.* 41, 7394–7401 (2015).
150. A.R. Chavan, J.S. Kounsalye, R.R. Chilwar, S.B. Kale, and K.M. Jadhav, Cu^{2+} substituted $NiFe_2O_4$ thin films via spray pyrolysis technique and their high-frequency devices application. *J. Alloy. Compd.* 769, 1132–1145 (2018).
151. H.J. Kardile, S.B. Somvanshi, A.R. Chavan, A.A. Pandit, and K.M. Jadhav, Effect of Cd^{2+} doping on structural, morphological, optical, magnetic and wettability properties of nickel ferrite thin films. *Optik* 207, 164462 (2020).
152. L. Avazpour, M.R. Toroghinejad, and H. Shokrollahi, Enhanced magneto-optical Kerr effect in rare earth substituted nanostructured cobalt ferrite thin film prepared by sol–gel method. *Appl. Surf. Sci.* 387, 869–874 (2016).
153. V.G. Harris, N.C. Koon, C.M. Williams, Q. Zhang, M. Abe, and J.P. Kirkland, Cation distribution in NiZn-ferrite films via extended x-ray absorption fine structure. *Appl. Phys. Lett.* 68, 2082–2084 (1996).
154. H. Yao, X. Ning, H. Zhao, A. Hao, and M. Ismail, Effect of Gd-doping on structural, optical, and magnetic properties of $NiFe_2O_4$ As-prepared thin films via facile sol-gel approach. *ACS Omega* 6, 6305–6311 (2021).
155. R. Galindo, E. Mazario, S. Gutiérrez, M.P. Morales, and P. Herrasti, Electrochemical synthesis of $NiFe_2O_4$ nanoparticles: characterization and their catalytic applications. *J. Alloy. Compd.* 536, S241–S244 (2012).
156. S. Maensiri, M. Sangmanee, and A. Wiengmoon, Magnesium ferrite ($MgFe_2O_4$) nanostructures fabricated by electrospinning. *Nanoscale Res. Lett.* 4, 221 (2008).
157. G. van der Laan, and A.I. Figueroa, X-ray magnetic circular dichroism—a versatile tool to study magnetism. *Coord. Chem. Rev.* 277–278, 95–129 (2014).
158. W. Baaziz, B.P. Pichon, Y. Liu, J.-M. Grenèche, C. Ulhaq-Bouillet, E. Terrier, N. Bergeard, V. Halté, C. Boeglin, F. Choueikani, M. Toumi, T. Mhiri, and S. Begin-Colin, Tuning of synthesis conditions by thermal decomposition toward core–shell $Co_xFe_{1-x}O@Co_yFe_{3-y}O_4$ and $CoFe_2O_4$ nanoparticles with spherical and cubic shapes. *Chem. Mater.* 26, 5063–5073 (2014).
159. S. Nappini, E. Magnano, F. Bondino, I. Píš, A. Barla, E. Fantechi, F. Pineider, C. Sangregorio, L. Vaccari, L. Venturelli, and

P. Baglioni, Surface charge and coating of $CoFe_2O_4$ nanoparticles: evidence of preserved magnetic and electronic properties. *J. Phys. Chem. C* 119, 25529–25541 (2015).

160. J.M. Byrne, V.S. Coker, E. Cespedes, P.L. Wincott, D.J. Vaughan, R.A.D. Pattrick, G. van der Laan, E. Arenholz, F. Tuna, M. Bencsik, J.R. Lloyd, and N.D. Telling, Biosynthesis of Zinc substituted magnetite nanoparticles with enhanced magnetic properties. *Adv. Func. Mater.* 24, 2518–2529 (2014).
161. J.P. Singh, B. Kaur, A. Sharma, S.H. Kim, S. Gautam, R.C. Srivastava, N. Goyal, W.C. Lim, H.J. Lin, J.M. Chen, K. Asokan, D. Kanjilal, S.O. Won, I.-J. Lee, and K.H. Chae, Mechanistic insights into the interaction between energetic oxygen ions and nanosized $ZnFe_2O_4$: XAS-XMCD investigations. *Phys. Chem. Chem. Phys.* 20, 12084–12096 (2018).
162. J.F. Hochepied, P. Sainctavit, and M.P. Pileni, X-ray absorption spectra and X-ray magnetic circular dichroism studies at Fe and Co $L_{2,3}$ edges of mixed cobalt–zinc ferrite nanoparticles: cationic repartition, magnetic structure and hysteresis cycles. *J. Magn. Magn. Mater.* 231, 315–322 (2001).
163. N. Daffé, F. Choueikani, S. Neveu, M.-A. Arrio, A. Juhin, P. Ohresser, V. Dupuis, and P. Sainctavit, Magnetic anisotropies and cationic distribution in $CoFe_2O_4$ nanoparticles prepared by coprecipitation route: Influence of particle size and stoichiometry. *J. Magn. Magn. Mater.* 460, 243–252 (2018).
164. M.Y. Yang, S. Seong, E. Lee, M. Ghanathe, A. Kumar, S.M. Yusuf, Y. Kim, and J.-S. Kang, Electronic structures and magnetization reversal in $Li_{0.5}FeCr_{1.5}O_4$. *Appl. Phys. Lett.* 116, 252401 (2020).
165. K. Ugendar, V. Hari Babu, V. Raghavendra Reddy, and G. Markaneyulu, Cationic ordering and magnetic properties of rare-earth doped $NiFe_2O_4$ probed by Mössbauer and x-ray spectroscopies. *J. Magn. Magn. Mater.* 484, 291–297 (2019).
166. P. Mendoza Zélis, G.A. Pasquevich, K.L. Salcedo Rodríguez, F.H. Sánchez, and C.E. Rodríguez Torres, Surface magnetic contribution in zinc ferrite thin films studied by element- and site-specific XMCD hysteresis-loops. *J. Magn. Magn. Mater.* 419, 98–104 (2016).
167. S. Matzen, J.B. Moussy, R. Mattana, K. Bouzehouane, C. Deranlot, F. Petroff, J.C. Cezar, M.A. Arrio, P. Sainctavit, C. Gatel, B. Warot-Fonrose, and Y. Zheng, Epitaxial growth and ferrimagnetic behavior of $MnFe_2O_4(111)$ ultrathin layers for room-temperature spin filtering. *Phys. Rev. B* 83, 184402 (2011).
168. K.L. Salcedo Rodríguez, G. Bridoux, S.P. Heluani, G.A. Pasquevich, P.D. Esquinazi, and C.E. Rodríguez Torres, Influence of substrate effects in magnetic and transport properties of magnesium ferrite thin films. *J. Magn. Magn. Mater.* 469, 643–649 (2019).
169. S. Emori, D. Yi, S. Crossley, J.J. Wisser, P.P. Balakrishnan, B. Khodadadi, P. Shafer, C. Klewe, A.T. N'Diaye, B.T. Urwin, K. Mahalingam, B.M. Howe, H.Y. Hwang, E. Arenholz, and Y. Suzuki, Ultralow damping in nanometer-thick epitaxial spinel ferrite thin films. *Nano Lett.* 18, 4273–4278 (2018).
170. S. Emori, B.A. Gray, H.-M. Jeon, J. Peoples, M. Schmitt, K. Mahalingam, M. Hill, M.E. McConney, M.T. Gray, U.S. Alaan, A.C. Bornstein, P. Shafer, A.T. N'Diaye, E. Arenholz, G. Haugstad, K.-Y. Meng, F. Yang, D. Li, S. Mahat, D.G. Cahill, P. Dhagat, A. Jander, N.X. Sun, Y. Suzuki, and B.M. Howe, Coexistence of low damping and strong magnetoelastic coupling in epitaxial spinel ferrite thin films. *Adv. Mater.* 29, 1701130 (2017).
171. J. Thien, J. Bahlmann, A. Alexander, K. Ruwisch, J. Rodewald, T. Pohlmann, M. Hoppe, F. Alarslan, M. Steinhart, B. Altuncevahir, P. Shafer, C. Meyer, F. Bertram, J. Wollschläger, and K. Küpper, Cationic ordering and its influence on the magnetic properties of Co-rich cobalt ferrite thin films prepared by reactive solid phase epitaxy on Nb-doped SrTiO3(001). *Materials* 15, 46 (2022).
172. Murad, E., Chapter 2.1 - Mössbauer Spectroscopy. In *Developments in Clay Science*, Bergaya, F.; Lagaly, G., Eds. Elsevier: 2013; Vol. 5, pp 11–24.
173. G.A. Sawatzky, F. Van Der Woude, and A.H. Morrish, Recoil-less-fraction ratios for Fe^{57} in octahedral and tetrahedral sites of a spinel and a garnet. *Phys. Rev.* 183, 383–386 (1969).
174. V.K. Mittal, P. Chandramohan, S. Bera, M.P. Srinivasan, S. Velmurugan, and S.V. Narasimhan, Cation distribution in $Ni_xMg_{1-x}Fe_2O_4$ studied by XPS and Mössbauer spectroscopy. *Solid State Commun.* 137, 6–10 (2006).
175. D. Carta, M.F. Casula, G. Mountjoy, and A. Corrias, Formation and cation distribution in supported manganese ferrite nanoparticles: an x-ray absorption study. *Phys. Chem. Chem. Phys.* 10, 3108–3117 (2008).
176. D. Carta, D. Loche, G. Mountjoy, G. Navarra, and A. Corrias, $NiFe_2O_4$ nanoparticles dispersed in an aerogel silica matrix: an x-ray absorption study. *J. Phys. Chem. C* 112, 15623–15630 (2008).
177. T.A.S. Ferreira, J.C. Waerenborgh, M.H.R.M. Mendonça, M.R. Nunes, and F.M. Costa, Structural and morphological characterization of $FeCo_2O_4$ and $CoFe_2O_4$ spinels prepared by a coprecipitation method. *Solid State Sci.* 5, 383–392 (2003).
178. C.N. Chinnasamy, A. Narayanasamy, N. Ponpandian, K. Chattopadhyay, K. Shinoda, B. Jeyadevan, K. Tohji, K. Nakatsuka, T. Furubayashi, and I. Nakatani, Mixed spinel structure in nanocrystalline $NiFe_2O_4$. *Phys. Rev. B* 63, 184108 (2001).